Three-dimensional direct numerical simulation of a turbulent lifted hydrogen jet flame in heated coflow: Flame stabilization and structure

C. S. YOO[1], R. SANKARAN[2] AND J. H. CHEN[1]

[1]Combustion Research Facility, Sandia National Laboratories, Livermore, CA 94550-0969, USA

[2]National Center for Computational Sciences, Oak Ridge National Laboratories, Oak Ridge, TN 37831-06008, USA

(Received ?? and in revised form ??)

Direct numerical simulation (DNS) of the near field of a three-dimensional spatially-developing turbulent lifted hydrogen jet flame in heated coflow is performed with a detailed mechanism to determine the stabilization mechanism and the flame structure. The DNS was performed at a jet Reynolds number of 11 000 with over 940 million grid points. The results show that auto-ignition in a fuel-lean mixture at the flame base is the main source of stabilization of the lifted jet flame. A chemical flux analysis shows the occurrence of near-isothermal chemical chain branching preceding thermal runaway upstream of the stabilization point, indicative of hydrogen auto-ignition in the second limit. The Damköhler number and key intermediate species behavior near the leading edge of the lifted flame also verify that auto-ignition occurs at the flame base. At the lifted flame base, it is found that heat release occurs predominantly through ignition where the gradients of reactants are opposed. Downstream of the flame base, both rich-premixed and non-premixed flames develop and coexist with auto-ignition. In addition

to auto-ignition, Lagrangian tracking of the flame base reveals the passage of large-scale flow structures and their correlation with the fluctuations of the flame base. In particular, the relative position of the flame base and the coherent flow structure induces a cyclic motion of the flame base in the transverse and axial directions about a mean lift-off height. This is confirmed by Lagrangian tracking of key scalars, heat release rate, and velocity at the stabilization point.

---

1. Introduction

Turbulent lifted jet flames have been widely investigated due to their importance in both practical applications including direct injection stratified spark ignition engines, diesel engines and commercial boilers, and also as a building-block configuration for understanding partial-premixing and auto-ignition in turbulent combustion. In particular, the stabilization mechanism of a lifted flame base has drawn great attention because the lifted flame base determines the overall flame stability and characteristics of combustion systems (e.g. Peters 2000). For example, broadband chemiluminescence measurements have shown the contribution of low-temperature ignition kinetics in stabilizing a lifted diesel jet flame (e.g. Dec 1997; Pickett *et al.* 2005). Despite the practical importance of flame base stabilization, however, thus far there has been little consensus among researchers regarding the dominant mechanism which stabilizes a lifted flame base, not only because of the complex structure and propagation characteristics of turbulent lifted flames, but also because of the difficulty in obtaining simultaneous time-resolved, time-series measurements of key scalar and velocity fields.

Various theories have been proposed to explain the stabilization mechanism of turbulent lifted jet flames, which can broadly be categorized based on the premixedness of

the mixture upstream of the flame base, or on the effect of local turbulence structure. Depending upon the degree of fuel-air premixing upstream of the flame base, theories can be classified as: premixed flame theory (e.g. Vanquickenborne & van Tiggelen 1966; Kalghatgi 1984), non-premixed flamelet theory (e.g. Peters & Williams 1983), and edge flame theory (e.g. Muñiz & Mungal 1997; Upatnieks *et al.* 2004; Joedicke *et al.* 2005; Buckmaster 2002; Chung 2007). They can also be categorized based on the local turbulence effect on the flame base; i.e. turbulence intensity theory (e.g. Kalghatgi 1984; Joedicke *et al.* 2005) and large eddy theory (e.g. Miake-Lye & Hammer 1988; Tacke *et al.* 1998; Su *et al.* 2006). Readers are referred to comprehensive reviews by Lyons (2007) and Pitts (1998) for details of the theories.

Recently, auto-ignition was proposed as another important stabilization mechanism of lifted flames in a heated coflow (e.g. Dec 1997; Cabra *et al.* 2002; Markides & Mastorakos 2005; Gordon *et al.* 2008). Since auto-ignition can assist in stabilizing a turbulent flame base, re-circulating hot combustion products have been adopted in bluff-body or swirl-stabilized burners. For example, in diesel engines, fuel is injected and mixed with heated oxidizer in the chamber at temperatures exceeding the ignition limit. The lift-off height and overall characteristics of the lifted flame and soot processes are highly affected by the role of ignition on diesel jet flame stabilization (e.g. Pickett 2005).

In addition to the numerous experimental studies, stabilization characteristics of a lifted jet flame in a heated shear layer were investigated using a two-dimensional direct numerical simulation (DNS) with single-step global chemistry by Jiménez & Cuenot (2007), in which re-ignition triggered by re-circulating hot gas was found to be the key mechanism to stabilize the lifted triple flame along with the passage of large-scale flow structures. While providing qualitative insights regarding the roles of auto-ignition and edge propagation, this study did not include realistic timescales associated with igni-

tion kinetics relative to mixing time scales in a turbulent shear flow owing to the two-dimensional configuration and the simple chemistry. To address the ignition effect on the stabilization mechanism, there have been large eddy simulations (LES) and Reynolds-averaged Navier-Stokes (RANS) simulations with transported probability density function (PDF) methods applied to the experimental Cabra burner (e.g. Cabra *et al.* 2002; Masri *et al.* 2004; Cao *et al.* 2005; Gordon *et al.* 2007; Gkagkas & Lindstedt 2006; Jones & Navarro-Martinez 2007), in which the lift-off heights are predicted with reasonable accuracy. More recently, Domingo *et al.* (2008) investigated a lifted methane jet flame in a vitiated coflow using LES with tabulated chemistry for auto-ignition and premixed flamelets.

In the present study, the stabilization mechanism and flame structure of a turbulent lifted hydrogen jet flame in a heated coflow is investigated by performing three-dimensional DNS with detailed hydrogen-air chemistry. First, the role of auto-ignition resulting from the heated coflow is examined in detail by analyzing relevant elementary reactions occurring near the flame base to unambiguously determine the stabilization mechanism of the flame. In addition, the instantaneous and time-averaged flame structure and flow field in the vicinity of the flame base are characterized and their role in stabilization is elucidated. Flame structure at different axial locations is characterized by conditional flame index statistics. Finally, the role of the near-field, large-scale flow motion in the stabilization mechanism is elucidated by Lagrangian tracking of the flame base together with relevant scalar and velocity fields.

2. Problem configuration

The spatially-developing turbulent lifted jet flame simulation was performed in a three-dimensional slot-burner configuration. Fuel issues from a central jet, which consists of

65 % hydrogen and 35 % nitrogen by volume at an inlet temperature of $T_j = 400$ K. The central jet is surrounded on either side by co-flowing heated air streams at $T_c = 1100$ K and atmospheric pressure. This temperature exceeds the crossover temperature of hydrogen-air chemistry (e.g. Law 2006), such that the mixture upstream of the flame base is auto-ignitable. The mixture composition was selected such that the stoichiometric mixture fraction, $\xi_{\rm st} = 0.1990$, based on the formula of Bilger (1988), resides in a region of high shear in the developing jet. The mean inlet axial velocity, $U_{\rm in}$, is given by:

$$U_{\rm in} = U_c + \frac{U_j - U_c}{2}\left(\tanh\Big(\frac{y - H/2}{2\delta}\Big) + \tanh\Big(\frac{y - H/2}{2\delta}\Big)\right), \tag{2.1}$$

where U_c and U_j denote the mean coflow and mean inlet jet velocities, respectively. H is the jet width at the inlet and δ is specified as: $\delta = 0.05H$. The width of the fuel and temperature at the inlet is denoted by $H_\xi = H - \delta_\xi$ (figure 1), where $\delta_\xi = H/6$, and is slightly less than H such that $\xi_{\rm st}$ and $\xi_{\rm MR}$ are in the middle of the shear layer. $\xi_{\rm MR}$ is the most reactive mixture fraction (≈ 0.05 in this study) corresponding to the shortest homogeneous ignition delay (e.g. Mastorakos *et al.* 1997*a*). This configuration ensures maximum interaction between the lifted flame base and local turbulence. Moreover, for computational affordability and expediency, the choice of a large mean axial velocity and high temperature at $\xi_{\rm MR}$ provide sufficient lift-off height with a sufficiently short ignition delay such that the present DNS with a billion grid points is achievable using terascale high performance computing. Hence, this configuration may effectively render the present lifted jet flame equivalent to a flame with a larger $\xi_{\rm st}$.

The velocity fluctuation, u', is imposed on the mean inlet velocity. The fluctuation, u', is obtained by generating an auxiliary homogeneous isotropic turbulence field based on a prescribed energy spectrum as in Sankaran *et al.* (2007) and Yoo *et al.* (2005). The frozen velocity fluctuation field is added to the mean inlet velocity using the Taylor hypothesis. After an initial axial distance where the turbulence evolves from the imposed

spectrum, the turbulence intensity is $u'/U_j = 0.091$, the turbulence integral scale in the spanwise direction is $l_{33}/H = 0.37$, and the turbulent Reynolds number is $Re_t = 340$ on the jet centerline at $x = L_x/4$. Note that l_{33} is evaluated from an auto-correlation of the spanwise velocity. The numerical and physical parameters are summarized in table 1 and the mean inlet scalar and velocity profiles are shown in figure 1.

The computational domain is $12.5H \times 16.7H \times 3.3H$ in the streamwise, x, transverse, y, and spanwise, z, directions. A uniform grid spacing of 15 μm is used in the streamwise and spanwise directions, while an algebraically-stretched mesh is used in the transverse direction, obtained from $y(s) = f(s) \times L_y/2$, where s is the equi-spaced computational grid and $0 \leqslant s \leqslant 1$. The stretching function is given by:

$$f(s) = \beta s + \frac{1}{2}\left(1 + \tanh\frac{s - s^*}{\sigma}\right)\left(e^{ks} - \beta s\right), \tag{2.2}$$

where $k = \ln(s^*)/(s^* - 1)$, $\beta = 0.64$, $s^* = 0.80$, and $\sigma = 1/20$. To obtain a symmetric mesh, the mesh was mirrored across the jet centerline ($y = s = 0$). The resultant mesh provides a uniform grid spacing of 15 μm over an $8H$ wide region in the center of the domain. The width of the uniform-grid region in the transverse direction was carefully chosen to ensure that the instantaneous jet flame and mixing zone always remained well within the fine-mesh region of the domain. The mildly stretched mesh outside of the uniform grid region is intended to move the transverse boundary farther from the turbulent jet to avoid entrainment of fluid at the boundary into the domain without incurring prohibitive computational cost. Previous results (Sankaran *et al.* 2007) have demonstrated that the grid-stretching effect on the solution is negligible.

The fine grid spacing of 15 μm was necessary to resolve the internal flame structure under extinction strain conditions and to provide adequate resolution of the turbulence scales. Note that except for the core jet region near the jet exit ($x/H \leqslant 3$) where the Kolmogorov length scale, η_{K}, is resolved by half a grid point due to high intensity

turbulence, at least one grid point is located within the Kolmogorov length scale. The Kolmogorov length scale is defined as $\eta_{\mathrm{K}} = (\widetilde{\nu}^3/\widetilde{\epsilon})^{1/4}$ with $\widetilde{\epsilon}$ being the Favre mean turbulent dissipation rate and $\widetilde{\nu}$ being the Favre mean kinematic viscosity. The physical grid spacing for good resolution of the smallest scales in DNS is approximately $2\eta_{\mathrm{K}}$ (e.g. Pope 2000; Yeung & Pope 1989), such that the grid resolution in this study is sufficiently fine to resolve the smallest turbulence scales.

The compressible Navier–Stokes, species continuity, and total energy equations were solved using the Sandia DNS code, S3D (Chen *et al.* 2009). A fourth-order explicit Runge–Kutta method by Kennedy & Carpenter (1994) was used for time integration. The solution was spatially discretized using an eighth-order central differencing scheme and a tenth-order filter was used to remove any spurious high-frequency fluctuations in the solution (Kennedy *et al.* 2000). A detailed hydrogen-air kinetic mechanism composed of 9 species (H_2, O_2, O, OH, H_2O, H, HO_2, H_2O_2, and N_2) and 21 elementary reaction steps (Li *et al.* 2004) was used. For details regarding the hydrogen-air chemistry, readers are referred to table 2. CHEMKIN and TRANSPORT software libraries (Kee *et al.* 1996, 1986) were linked with S3D to evaluate reaction rates, thermodynamic and mixture-averaged transport properties.

Navier–Stokes characteristic boundary conditions (NSCBC) were used to prescribe the boundary conditions (Poinsot & Lele 1992). Improved non-reflecting inflow/outflow boundary conditions (Sutherland & Kennedy 2003; Yoo *et al.* 2005; Yoo & Im 2007) were used in the streamwise and transverse directions, and periodic boundary conditions were applied in the spanwise direction. Based on the prescribed inlet jet velocity and the streamwise domain length, a flow-through time, τ_j $(= L_x/U_j)$, is approximately 0.07 ms. The solution was advanced at a constant time step of 4 ns through $12\tau_j$ to provide stationary statistics. The simulation was performed on the Cray XT3/XT4 at

Oak Ridge National Laboratories and required 3.5 million CPU-hours running for 15 days on approximately 10 000 processors.

To facilitate the simulation, the central hydrogen/nitrogen jet was ignited by artificially imposing a high-temperature region in the central jet. The initially hot region was readily convected out of the domain by the fast central jet within one τ_j. After $t/\tau_j = 8$, the lifted jet flame base approached statistical stationarity, and fluctuated about its steady stabilization lift-off height, $\overline{h}$, of approximately $\overline{h}/H = 2.6$. Note that, near the flame base, time-averaged variables such as temperature and species mass fractions remain constant irrespective of the time averaging range. Downstream of $x/H \approx 5$, however, the statistical means vary slightly due to the intrinsic flapping motion of the jet, the slow convective velocity of the coflow, and marginal total simulation time compared with the flapping frequency.

3. General features of the turbulent lifted flame

The global structure of the flame stabilization base is revealed from instantaneous images of the flame structure at different times. Figure 2 shows three-dimensional volume renderings of scalar dissipation rate, χ, and the mass fraction of the hydroxyl (OH) and perhydroxyl (HO_2) radicals. Hydroxyl is often used as an experimental marker of the lifted flame base (e.g. Tacke *et al.* 1998; Schefer & Goix 1998; Cabra *et al.* 2002). The scalar dissipation rate, χ, is defined by $\chi = 2D|\boldsymbol{\nabla}\xi|^2$, where D is the local thermal diffusivity. At first glance, we identify that fine flow structures upstream of the flame base are readily dissipated as the flow traverses downstream, primarily due to the effect of heat release by the flame (e.g. Mueller *et al.* 1998). Moreover, the flame base appears highly irregular and is strongly affected by the instantaneous local flow and mixture conditions.

Therefore, the stabilization of the lifted jet flame is not a global phenomenon, but rather, a highly-localized phenomenon.

An overall description of the planar jet flow is given by the downstream evolution of the mean axial velocity, $\widetilde{U}$, and axial velocity fluctuation, u_1', shown in figure 3. Henceforth, $\widetilde{\phi}$ denotes the Favre mean of a variable, ϕ, defined as $\widetilde{\phi}(x,y) = \overline{\rho\phi}/\overline{\rho}$, where ρ is density and the overbar denotes ensemble averages. The ensemble average is defined as:

$$\overline{\phi}(x,y) = \frac{1}{N_t N_z} \sum_{n=1}^{N_t} \sum_{k=1}^{N_z} \phi(x,y,z_k,t_n), \tag{3.1}$$

where N_t is the number of data sets in a statistically stationary time period in the simulation between $8\tau_j$ and $12\tau_j$, and N_z is the number of grid points in the z–direction. The transverse direction is normalized by the jet half-width, $\delta_{1/2}$, which is defined as half of the transverse distance where the mean axial velocity, $\widetilde{U}$, exceeds 50 % of the corresponding mean axial velocity at the centerline, $\widetilde{U}_0(x)$. It is readily observed from figure 3 that the top-hat inlet velocity, $\widetilde{U}$, quickly develops into a self-similar profile by $x/H = 4.4$, similar to the non-reacting turbulent planar jet DNS by Stanley *et al.* (2002). The velocity fluctuation is highest in the middle of the shear layer ($y = \pm\delta_{1/2}$) due to the mean shear of the jet. Note that the fluctuations at the centerline remain relatively constant compared to fluctuations in the shear layers where most of the heat release is generated in the flame. Therefore, the jet core does not fully participate with the reaction layers and survives to the end of the domain.

The spreading of the jet is manifested by the downstream evolution of $\widetilde{U}_0(x)$ and $\delta_{1/2}$ presented in figure 4(a). Several other quantities such as $\overline{\rho}_0$, $\overline{\rho}_0\widetilde{U}_0^2\delta_{1/2}$, and the mean momentum flow rate, $\dot{M}$, are also presented in the figure, demonstrating that $\dot{M}$ in the turbulent reacting jet is conserved. $\dot{M}$ is defined as:

$$\dot{M} = \int_{-\infty}^{\infty} \overline{\rho}\widetilde{U}^2 \mathrm{d}y \simeq \overline{\rho}_0\widetilde{U}_0^2\delta_{1/2} \int_{-\infty}^{\infty} f(\psi)\mathrm{d}\psi, \tag{3.2}$$

where $f(\psi) \equiv \overline{\rho}\widetilde{U}^2/\overline{\rho}_0\widetilde{U}_0^2$ and $\psi = y/\delta_{1/2}$. It is readily observed that $\delta_{1/2}$ grows faster than the rate at which $\widetilde{U}_0$ and $\overline{\rho}_0$ decrease. The jet half-width, $\delta_{1/2}$, increases as the turbulent shear layer develops immediately downstream of the fuel jet nozzle, but $\widetilde{U}_0$ does not change significantly due to flow expansion and turbulent mixing. Moreover, $\delta_{1/2}$ is more directly affected by flow expansion due to the presence of the flame than $\widetilde{U}_0$ and $\overline{\rho}_0$ because the present lifted flame starts to develop in lean mixtures outside of the shear layer as will be discussed in the following paragraph. Note also that compared to the non-reacting jet studied by Stanley *et al.* (2002), $\widetilde{U}_0$ in the present reacting turbulent jet decreases minimally. Therefore, $\overline{\rho}_0\widetilde{U}_0^2\delta_{1/2}$ in (3.2) first increases with $\delta_{1/2}$, but then levels off and remains independent of x once a non-premixed flame develops downstream of the lifted flame base region. This is because $\overline{\rho}_0\widetilde{U}_0^2$ varies as x^{-1} while $\delta_{1/2}$ increases linearly with x. Therefore, from figure 4(b), it is observed that $\overline{\rho}\widetilde{U}^2$ becomes self-similar for $x/H \geqslant 5.0$, and hence, the momentum flow rate is conserved downstream of this position as shown in figure 4(a).

In addition to the flow characteristics, global characteristics of the lifted flame represented by the mean temperature, $\widetilde{T}$, and mean heat release rate, $\widetilde{\dot{q}}$, are presented in figure 5. Note that $\widetilde{\dot{q}}$ starts to increase slightly ahead of the lifted flame base ($x/H = 2.6$) and attains its maximum approximately at $x/H = 4$. Past this vigorous reaction region, $\widetilde{\dot{q}}$ decreases significantly and remains relatively constant. Subsequently, $\widetilde{T}$ increases following $\widetilde{\dot{q}}$ and levels off after $x/H = 6$. Note also that the local peak of $\widetilde{\dot{q}}$ occurs at $y = \pm 1.5\delta_{1/2}$ at the flame base, and subsequently shifts towards the centerline as the flame develops downstream. These results imply that highly transient reactions associated with auto-ignition first occur outside the shear region, followed by the development of a stable flame downstream.

Although the mean quantities provide a description of global features pertaining to

the characteristics of the turbulence and flame structures, the averaged information is insufficient to describe the dynamics of the lifted flame which is governed by local scalar fluctuations. Instantaneous snapshots of a two-dimensional x–y plane are extracted from the three-dimensional data. Figure 6 shows a typical temporal sequence of images of $Y_{\mathrm{OH}}, Y_{\mathrm{HO_2}}, T$, and χ isocontours at the leading edge of the lifted jet flame between $t/\tau_j = 8.43$ and 9.29 in the $z = 0$ plane. Note that the leading edge shown here corresponds to the left branch of the flame, and hence, the centerline of the fuel jet lies to the right of each figure (not shown in the figures). It is readily observed that, near the flame base, most of the OH radical is concentrated in a fuel-lean mixture where $\xi < \xi_{\mathrm{st}}$. It is also apparent that a pool of HO_2 exists upstream of the location where OH accumulates. The presence of HO_2 upstream of other intermediate species indicates the importance of auto-ignition in the stabilization of the lifted flame base (e.g. Cao *et al.* 2005; Law 2006; Echekki & Chen 2003; Gordon *et al.* 2007).

However, it is not clear how the flame base stabilizes in the presence of auto-ignition, especially in the mixture fraction coordinate. It is conceivable that the flame base coincides with ξ corresponding to the shortest ignition delay since auto-ignition appears to be the main source of the flame stabilization. In turbulent flows, however, ignition delay highly depends on the physicochemical path of a given ignition kernel and can be significantly longer, by a factor of two or greater, than the homogeneous ignition delay due to heat and radical losses induced by local mixing rates (e.g. Echekki & Chen 2003). Therefore, to understand the stabilization mechanism of a turbulent lifted jet flame, it is necessary to characterize the evolution of key scalars and velocity in the vicinity of the lifted flame base. For this purpose, we define the most upstream point of a scalar isoline that encompasses thermal runaway as the location of the lifted flame base, and henceforth, refer to it as the 'stabilization point'. The $Y_{\mathrm{OH}} = 0.001$ isoline was found to

be an excellent marker of this point. As shown in figure 6, the isoline of $Y_{\rm OH} = 0.001$ encompasses the region where the following conditions are met: temperature starts to increase, significant heat release commences, a significant high-temperature radical pool exists (i.e. OH, O, and H), and HO_2 vanishes. Note that in hydrogen-air chemistry, the induction process prior to the thermal runaway occurs under nearly isothermal condition during which HO_2 radical builds up and subsequently is converted to hydroxyl radicals during thermal runaway, and hence an HO_2 isoline is not a good marker for thermal runaway. An independent verification of the stabilization point definition is shown in figure 6 where the OH isoline lies nearly coincident with a temperature isoline denoted by $T = T_c(= 1100\ {\rm K}) + \Delta T(= 50\ {\rm K})$. Note that in both definitions, $\Delta T(= 50\ {\rm K})$ and $Y_{\rm OH} = 0.001$ represent approximately 5 % of their maximum increase in the domain consistent with definitions used in previous studies (e.g. Cabra *et al.* 2002; Cao *et al.* 2005; Domingo *et al.* 2008).

In the following sections, details of the lifted flame stabilization mechanism and flame structure will be presented in terms of: 1) the role of auto-ignition; 2) the instantaneous flame and flow structures at different axial and spanwise locations in the jet, along with conditionally averaged flame statistics, and 3) flame base dynamics and its correlation with local gas and flame displacement velocities and other key scalars including scalar dissipation rate, heat release rate, and mixture fraction.

4. Role of auto-ignition

To understand in detail the dynamics of the stabilization process at the flame base, the temporal evolution of the flame and flow characteristics are investigated. In figure 6, the local maxima of $Y_{\rm OH}$ and T are identified at several locations in the fuel-lean mixture, indicative of auto-ignition occurring locally. The local maxima are not a result of out-

of-plane motion in the spanwise direction, z. In general, propagating flames such as edge flames and premixed flames exhibit temperature or species profiles which evolve monotonically from unburned to burned gas temperature or from reactants to products. Therefore, the presence of several local maxima of temperature or species mass fraction across or along a flame is unlikely, unless local extinction occurs. In the present case, however, the scalar dissipation rate in the fuel-lean mixture is considerably less than the extinction scalar dissipation rate, χ^q, of the corresponding strained laminar non-premixed flame. Note that $\chi^q_{\rm st} \approx 10\,400\ s^{-1}$ at $\xi_{\rm st}$ $(= 0.1990)$ for this particular flame, evaluated using OPPDIF by Lutz *et al.* (1997) at the extinction point. For example, a representative developing ignition kernel denoted as 'A' at $t/\tau_j = 9.0$ exists upstream of the high-temperature region. At this location there is a local maximum in OH and a depletion of HO_2, the temperature is approximately 1300 K, and the scalar dissipation rate, $\chi \approx 100$ s^{-1}, is low. These aero-thermochemical conditions reveal the occurrence of auto-ignition. Therefore, at the flame base one mode of auto-ignition occurs under fuel-lean, hot mixtures such that combustion at the flame base occurs as spontaneous ignition (e.g. Zeldovich 1980). Though the front may resemble an edge flame, molecular transport in this combustion regime is negligible relative to reaction. In addition to the topology of the temperature and species fields, an independent verification of the presence of auto-ignition is obtained from the chemical signature of hydrogen ignition.

A reaction rate flux analysis is performed to determine the dominant chemistry occurring near the flame base. Figure 7 shows representative profiles of the elementary reaction rates of HO_2 and OH, and temperature at two axial locations along the lines denoted as 'a' and 'b' at $t/\tau_j = 9.0$ shown in figure 6. Upstream of the flame base (not shown here), the dominant production of HO_2 is by R9 ($H + O_2 + M \rightarrow HO_2 + M$) and its consumption is negligible such that HO_2 radicals accumulate. Near the flame base at

$x/H = 3.0$ (figure 7a), however, R11 ($HO_2 + H \rightarrow OH + OH$) balances R9 along with to a lesser degree R10 ($HO_2 + H \rightarrow H_2 + O_2$) and R12 ($HO_2 + O \rightarrow OH + O_2$), and hence, HO_2 approaches its chemical steady-state. Therefore, the chain branching by R11 with R9 upstream of the flame base contributes to the production of OH and eventually induces thermal runaway. These characteristics of the elementary reactions can be observed during the chemical induction phase of auto-ignition preceding thermal runaway (e.g. Kreutz & Law 1996; Helenbrook *et al.* 1998; Im *et al.* 1998; Echekki & Chen 2003), and thus, indicate that auto-ignition occurs near the flame base.

Downstream of the flame base at $x/H = 4.4$ (figure 7b), R11 balances R9 at two transverse locations as manifested by the distinct peaks in the reaction rates. The first peak centered at $y/H = -1.2$ shows the production and consumption of HO_2 in a flame, and the second peak at $y/H = -0.4$ coincides with an ignition kernel evolving in a fuel-lean mixture which has been distorted by the intense turbulence in the central jet such that what is observed is its projection protruding out of a neighboring z–plane. The distinction between auto-ignition and flame chemistry can clearly be observed in the elementary reactions of OH. Note that at the location of the ignition kernels during the induction phase, the contribution of R11 ($HO_2 + H \rightarrow OH + OH$) to OH production becomes comparable to or even larger than the high-temperature chain-branching reactions, R1 ($H + O_2 \rightarrow O + OH$) and R2 ($O + H_2 \rightarrow OH + H$) (see figure 7$a$). However, in the high-temperature region the contribution of R11 to OH production is relatively small compared to R1 and R2; hence, the first temperature peak in figure 7(b) corresponds to a flame and not an ignition kernel. The axial distance between 'a' and 'b' in figure 6 suggests that one jet width is the nominal separation distance between auto-ignition at the flame base and its transition to a high-temperature flame.

A statistical view of the auto-ignition process at the flame base is presented in terms

of conditional statistics, useful for model development and validation. The conditional Favre mean, $\langle\phi|\xi^*\rangle$, and variance, $G_{\phi\phi}$, of a variable, ϕ, are defined as:

$$\langle\phi|\xi^*\rangle(x) = \frac{\sum_{n=1}^{N_t}\sum_{k=1}^{N_z}\sum_{j=1}^{N_y}(\rho(x,y_j,z_k,t_n)\phi(x,y_j,z_k,t_n)|\xi=\xi^*)}{\sum_{n=1}^{N_t}\sum_{k=1}^{N_z}\sum_{j=1}^{N_y}(\rho(x,y_j,z_k,t_n)\mid\xi=\xi^*)}, \tag{4.1}$$

$$G_{\phi\phi} = \langle\phi''\phi''|\xi^*\rangle, \tag{4.2}$$

where ξ^* is the sample space for ξ and $\phi'' = \phi - \langle\phi|\xi^*\rangle$ is the fluctuation of the variable. Henceforth, conditional mean and root mean square (r.m.s.) denote the conditional Favre mean and the r.m.s. of the conditional Favre variance, respectively.

Figure 8 shows the conditional mean and r.m.s. of temperature and a progress variable, c, defined as $c = Y_{\mathrm{H_2O}}/Y^{Eq}_{\mathrm{H_2O}}(\xi)$, where $Y^{Eq}_{\mathrm{H_2O}}$ is $Y_{\mathrm{H_2O}}$ at equilibrium. In this study, the progress variable is evaluated, providing useful data for turbulent combustion models which transport a progress variable and mixture fraction. $\langle T|\xi^*\rangle$ first increases in a fuel-lean mixture and subsequently the peak shifts towards richer mixtures. In the same way, $\langle c|\xi^*\rangle$ initially increases at the flame base and exceeds unity downstream of $x/H = 4.4$ in fuel-lean mixtures. Super-equilibrium values of $Y_{\mathrm{H_2O}}$ result from the ignition process. Further downstream, $\langle c|\xi^*\rangle$ in rich mixtures (centered at $\xi^* \sim 0.4$) approaches unity, which is also attributed to ignition occuring in rich mixtures. However, $\langle c|\xi^*\rangle$ near the stoichiometric mixture is always less than unity due to incomplete reaction caused by excessive mixing rates. Together with the chemical flux analysis at the flame base, these flame characteristics clearly indicates that ignition occurs first under hot, fuel-lean conditions where ignition delays are shorter, consistent with previous two-dimensional DNS of auto-ignition in an inhomogeneous hydrogen/air mixture (e.g. Echekki & Chen 2003) and turbulent mixing flows (e.g. Mastorakos *et al.* 1997*a*).

To quantitatively determine the relative importance of auto-ignition with turbulent mixing on the stabilization mechanism, the scalar dissipation rate, χ, and the Damköhler

number, Da, are investigated to isolate each effect. While the build-up of HO_2 upstream of other intermediate species (H, OH, and O) and the analysis of the elementary reactions provides evidence of auto-ignition at the flame base, Da defined as the ratio of species reaction term to diffusion provides a measure of the local residence time required for ignition. Significant losses of heat and radicals due to high χ can impede or cause ignition to slow down or cease (e.g. Echekki & Chen 2003) as manifested by small values of $Da \sim O(< 1)$. In this study, H_2O is chosen to evaluate Da since the rapid growth of H_2O at the expense of a near constant dissipative loss provides independent evidence of ignition. Da based on species k, is defined as (e.g. Echekki & Chen 2003):

$$Da = \frac{\dot{\omega}_k}{|-\partial/\partial x_j(\rho Y_k V_{j,k})|}, \tag{4.3}$$

where $V_{j,k}$ and $\dot{\omega}_k$ denote a diffusive velocity in the j direction and a net production rate of species k, respectively.

The conditional mean and r.m.s. values for χ and Da are presented in figure 9. It is of interest to note that except for very rich conditions, $\langle\chi|\xi^*\rangle$ is substantially lower than the extinction scalar dissipation rate, χ^q, of a strained laminar non-premixed flame, even near the fuel jet nozzle, and becomes an order of magnitude smaller than χ^q near the flame base. From this perspective, the non-premixed flamelet theory which conjectures that a lifted flame stabilizes where the local scalar dissipation rate decreases below a critical value, or χ^q, is clearly not the mechanism by which the present flame stabilizes. This problem with the non-premixed flamelet theory was previously discussed in Peters (2000).

In the present case, however, the ignition scalar dissipation rate, χ^i, should also be considered to understand the stabilization mechanism. As shown in figure 9(a), we notice that $\langle\chi|\xi^*\rangle$ at $\xi_{\rm MR}$ (≈ 0.05) is three times greater than χ^i ($\chi^i_{\rm MR} \approx 43$ s^{-1} at $\xi_{\rm MR}$) corresponding to a strained laminar non-premixed flame. Therefore, consideration of

only $\langle\chi|\xi^*\rangle$ would imply that auto-ignition cannot occur due to its high value. However, the r.m.s. of scalar dissipation rate, $G_{\chi\chi}^{1/2}$, is comparable to or even greater than $\langle\chi|\xi^*\rangle$ at ξ_{MR} along the axial direction. Thus, it is conceivable that auto-ignition can occur at a mixture fraction near ξ_{MR} if the local instantaneous value of scalar dissipation rate decreases below the corresponding χ^i and remains below this value for a sufficient length of time, consistent with previous results with global single-step chemistry (e.g. Mastorakos *et al.* 1997*a*,*b*).

Unlike the statistical characteristics of χ, $\langle Da|\xi^*\rangle$ in figure 9(*b*) shows that auto-ignition can be the main source of stabilization of the lifted flame, since its value for a lean mixture at the flame base is larger than unity, and its variance is considerably larger than the conditional mean. Downstream of the flame base at $x/H = 4.4$, the peak of $\langle Da|\xi^*\rangle$, which is still greater than unity, shifts towards fuel-rich mixtures, suggesting that auto-ignition also occurs in fuel-rich mixtures, whereas normal flames are developing near stoichiometric conditions. Further downstream, $\langle Da|\xi^*\rangle$ approaches unity near stoichiometric conditions and at fuel-rich mixtures with relatively small variances. This indicates a transition from auto-ignition to premixed or non-premixed flames where reaction counter-balances diffusion.

To further understand the characteristics of χ and Da, their PDFs, $P(\chi^*)$ and $P(Da^*)$, are evaluated at different locations and presented in figure 10. The PDFs of ξ and c are also presented in the figure. It is observed that at the mean stabilization position ($x/H = 2.6,\ y/H = -1.0$), the mean scalar dissipation rate, $\overline{\chi}$, is approximately 14 s^{-1} and its variance is 32 s^{-2}. This is a limited range considering that χ varies between 0 and values exceeding 10 000 s^{-1}. The corresponding mean mixture fraction, $\overline{\xi}$, is approximately 0.053 which is similar to ξ_{MR} (≈ 0.05). The mean Da, $\overline{Da}$, at the flame base is approximately 2.7 and the probability of $Da > 1$ is greater than 0.82, which indicates that the probability of

the occurrence of auto-ignition at the flame base is greater than the probability of flame propagation. These results are consistent with the previous discussion and clearly show that the mean stabilization point is a location favorable to auto-ignition substantiated by low $\overline{\chi}$ compared to χ^i, $\overline{Da}$ larger than unity, and $\overline{\xi}$ close to ξ_{MR}. Note that since auto-ignition is inherently a Lagrangian process following a specific fluid parcel, Eulerian means and PDFs evaluated at given locations do not provide cumulative history effects of mixing rates on ignition. Nonetherless, these statistics can characterize ignition at the flame base and provide useful validation data for Eulerian-based combustion models (e.g. the conditional moment closure (CMC) and flamelet models). The importance of the second-order moments to accurately model the conditional reaction rates was recently investigated using the present lifted-flame data (Richardson *et al.* 2009).

The downstream PDFs of χ, Da, ξ, and c are also presented in figure 10 along with a comparison with Gaussian and β-function PDFs, two commonly assumed functional forms for mixture fraction and progress variable in the presumed PDF approach (e.g. Bilger 1979; Borghi 1988; Peters 2000). It is readily observed that $P(\chi^*)$ follows the Gaussian distribution more closely with a slight negative skewness further downstream in the jet. Similar characteristics of $P(\chi^*)$ have been observed in previous experiments (Su & Clemens 2003) and DNS (Eswaran & Pope 1988). In flamelet and CMC models with the presumed shape PDF approach, the PDFs of mixture fraction and progress variable have often been assumed to have the functional form of the β-function (e.g. Peters 2000; Domingo *et al.* 2008). As shown in figure 10, both $P(\xi^*)$ and $P(c^*)$ follow the β-functions reasonably well, which implies that the presumed PDF approach may be valid as long as the transported mixture fraction, progress variable, and their variances are accurately calculated from LES or RANS.

5. Flame structure - degree of mixedness and burning mode

The turbulent lifted jet flame in heated coflow is an archetypical configuration to investigate not only flame stabilization, but also the complex flame structure resulting from auto-ignition, partial-premixing, and flame propagation in a dissipative environment. In this section the flame index, defined as the alignment of the fuel and oxidizer gradients, is used to determine the degree of mixedness. Together with the flame index, the heat release rate and Damköhler number of a reactive species are used to determine the burning mode. Collectively, these measures provide a way to delineate the various burning modes in the near field of the lifted flame - auto-ignition, flame propagation, and non-premixed flames.

The flame index has been used to distinguish premixed flames from non-premixed flames in turbulent non-premixed jet flames since it was first proposed by Yamashita *et al.* (1996). Employing the flame index, Mizobuchi *et al.* (2002) observed non-premixed, lean-premixed, and rich-premixed flames at the flame base from three-dimensional DNS of a turbulent lifted hydrogen jet flame in a quiescent ambient air. Rich-premixed flames and non-premixed flame islands were reported downstream of the flame base. From two-dimensional DNS of a turbulent lifted flame in heated air (Domingo *et al.* 2005), however, only non-premixed flames were observed upstream of where an edge-flame structure develops, similar to experiments (e.g. Choi & Puri 2000; Chung 2007).

In this study the normalized flame index, FI, is used, defined as:

$$FI = \frac{\boldsymbol{\nabla} Y_F \cdot \boldsymbol{\nabla} Y_O}{|\boldsymbol{\nabla} Y_F||\boldsymbol{\nabla} Y_O|}, \tag{5.1}$$

where the subscripts F and O represent fuel and oxidizer, respectively. Note that FI represents the cosine of the angle between the fuel and oxidizer gradients, and thus, values of FI close to unity imply aligned gradients, or 'aligned mixing' mode, while

negative values close to unity imply opposed gradients, or 'opposed mixing' mode. Note that, in the present study unlike in previous studies, the flame index is used only to measure the mixedness of the flow, and not to distinguish premixed and non-premixed flames.

Figure 11 shows isocontours of the heat release rate with the isoline of $\xi_{\rm st}$ $(= 0.1990)$ at different axial locations in the lifted jet flame. FI is also superimposed in the figure to determine the mixing mode. Near the flame base $(x/H = 2.6)$, the peak heat release rate occurs in a fuel-lean mixture where the gradients of the reactants are still largely opposed in the very near field. By $x/H = 3.4$, the peak heat release rate has migrated from fuel-lean conditions to near $\xi_{\rm st}$ and the reactants have had sufficient time to mix, hence their gradients are primarily aligned. At $x/H = 4.4$, the peak heat release rate has migrated toward much richer mixtures, and reaction occurs in both aligned and opposed mixing modes. Further downstream (at $x/H = 9.4$), heat release occurs in both fuel-rich and stoichiometric mixtures. In fuel-rich mixtures, the reactants are well mixed and their gradients are aligned, whereas near stoichiometric conditions, reaction is mixing limited, as the fuel and oxidizer gradients are opposed.

The axial mixedness of the jet flame is presented in terms of the conditional mean values for $\dot{q}$ and FI in figure 12. There are several interesting points to note about their downstream evolution. First, there is a shift in the peak $\langle \dot{q}|\xi^* \rangle$ from lean to rich mixtures along the axial direction. Second, the peak $\langle \dot{q}|\xi^* \rangle$ occurs at stoichiometric to slightly rich conditions within a jet-width downstream of the stabilization point and rapidly decreases further downstream. Third, two peaks in $\langle \dot{q}|\xi^* \rangle$ form further downstream of the flame base $(x/H = 9.4)$; one centered near stoichiometric and the second centered in fuel-rich conditions at a mixture fraction of ~ 0.6.

In terms of mixedness, near the flame base $(x/H = 2.6)$, $\langle FI|\xi^* \rangle$ indicates that heat

release occurs predominantly in fuel-lean mixtures where the gradients of fuel and oxidizer are largely opposed. However, by $x/H = 4.4$, there is a significant increase in heat release rate for stoichiometric and fuel-rich mixtures where the reactants are well-mixed and their gradients are aligned. Further downstream, consistent with the conditional heat release statistics, both aligned and opposed mixing modes prevail near stoichiometric and fuel-rich mixtures, respectively. The flame structure downstream of the flame base is consistent with previous DNS of a turbulent lifted jet flame in heated air and an experiment of partially premixed flames (e.g. Domingo *et al.* 2005; Choi & Puri 2000).

To further investigate the relation between the flame index and heat release rate, the mean of heat release rate conditional on $FI = FI^*$, or $\langle \dot{q}|FI^* \rangle$ is presented in figure 13. In addition, the heat release-weighted PDF of the flame index, $P_{\dot{q}}(FI^*)$ is also presented in the figure. $P_{\dot{q}}(FI^*)$ is defined as:

$$P_{\dot{q}}(FI^*; x) = \frac{\langle \dot{q}|FI^* \rangle P(FI^*; x)}{\bar{\dot{q}}}, \tag{5.2}$$

such that $P_{\dot{q}}(FI^*)$ represents the fraction of heat release rate at $FI = FI^*$, where $P(FI^*)$ denotes the PDF of the flame index. Note that $\langle \dot{q}|FI^* \rangle$ increases nearly linearly with the flame index and exhibits its peak when the reactant gradients are aligned for all axial locations. The peak heat release rate is nearly 4 to 5 times larger when the reactant gradients are aligned. The heat release weighted PDF of flame index, $P_{\dot{q}}(FI^*)$, however, shows a clear bimodal combustion behavior downstream of the flame base ($x/H > 2.6$). Upstream of the flame base, heat release rate is primarily generated where the reactant gradients are opposed due to its high probability in spite of the small $\langle \dot{q}|FI^* \rangle$. Note also that near the flame base, over 80 % of the heat release is generated where the reactant gradients are opposed. However, further downstream at $x/H = 4.4$, almost half of heat release (~ 47 %) is generated where the reactant gradients are aligned, such that both aligned and opposed mixing modes contribute nearly equally to the generation of

heat release. Past this vigorous reaction region, the fraction of the heat release rate from the opposed mixing mode increases again, accounting for up to 60 % of the total heat generation at $x/H = 9.4$. Thus, it can be expected that heat generation in the far-field of the jet flame is from mixing-limited non-premixed flames as in typical non-premixed jet flames.

Although a significant fraction of heat is from the opposed mixing mode at the flame base, it does not imply that non-premixed flames account for all of the heat release. Auto-ignition can also occur in mixtures for which the flame index is negative. To identify the contribution of ignition to the heat release along the axial direction, the mean heat release rate conditional on $Da = Da^*$, $\langle \dot{q}|Da^* \rangle$, and the heat release-weighted PDF of Da, $P_{\dot{q}}(Da^*)$, are evaluated and presented in figure 14. Note that $P_{\dot{q}}(Da^*)$ represents the fraction of heat release rate at $Da = Da^*$. Two points should be noted from $\langle \dot{q}|Da^* \rangle$. First, for $Da^* < 0.1$, $\langle \dot{q}|Da^* \rangle$ is nearly zero at all axial locations; therefore, reaction does not proceed when there is insufficient residence time, i.e. small values of Da^*, as expected. However, for $Da^* > 0.1$, $\langle \dot{q}|Da^* \rangle$ first increases rapidly with Da^* and then, levels off and remains relatively constant for $Da^* > 2$ at all axial locations. Therefore, $\langle \dot{q}|Da^* \rangle$ during an ignition process ($Da^* \gg 1$) is greater than from a normal flame ($Da^* \sim 1$), and moreover, $\langle \dot{q}|Da^* \rangle$ associated with ignition is nearly independent of Da^*. Second, the overall level of $\langle \dot{q}|Da^* \rangle$ increases rapidly within one to two jet widths downstream of the flame base ($x/H = 2.6$) and subsequently, decreases down to the level at the flame base as previously shown in figures 5 and 13. The statistics $P_{\dot{q}}(Da^*)$ shows that, at the flame base, approximately 77 % of the heat is released from the ignition mode ($Da^* > 1$). However, further downstream, the fraction of heat release from the ignition mode is significantly reduced, down to 35 % by $x/H = 9.4$. An inspection of the mean FI conditional on Da, $\langle FI|Da^* \rangle$, indicates that $\langle FI|Da^* \rangle$ is close to negative

unity for $Da^* > 1$ at the flame base. Hence, we can conclude that auto-ignition occurs primarily in the opposed mixing mode at the flame base.

In summary, near the stabilization point, the statistics of the flame index and Damköhler number show that auto-ignition occurs where the fuel and oxidizer gradient are opposed in fuel-lean mixtures. This is primarily due to the selection of the coflow temperature of 1100 K, which is considerably above the cross-over temperature for ignition. Hence, the flame stabilizes near the nozzle where significant premixing of fuel and oxidizer streams has not yet occurred. For lower coflow temperatures approaching the cross-over temperature, the flame will likely stabilize further downstream where a greater degree of premixing has occurred; therefore, it is conceivable that the heat release at the flame base may be either in a region of strong mixedness or in a region that exhibits both aligned and opposed mixing modes. Hence, the ignition and flame structure is likely to depend upon the competition between fuel-air mixing and ignition delay. For the present DNS conditions, downstream of the flame base, the conventional non-premixed and fuel-rich premixed flames develop; however, the fuel-lean premixed flame is negligible, even near the flame base. Note also that the extent of the domain encompasses only the near field of the jet; hence, the transition to a non-premixed flame in the absence of a premixed flame is not attained in the present simulation. Therefore, at the downstream boundary of the domain the fuel core jet still exists and hence, fuel-rich premixed flames are also sustained by the core jet.

6. Flame base dynamics

The previous sections have demonstrated that the main stabilization mechanism of the present lifted jet flame is auto-ignition of the fuel-lean mixture by the heated coflow, and auto-ignition occurs in the non-premixed mode where the fuel and oxidizer gradients

are not aligned. However, the flame base is also observed to fluctuate both spatially and temporally around a statistically stationary position. In this section, the source of the fluctuations is identified, especially as it relates to the underlying organized flow motion and mixing in jets, and its relation to intermittent ignition events.

In general, the stabilization point can be defined as the most upstream point of a particular isosurface of temperature or an intermediate species mass fraction in the computational domain. However, the stabilization mechanism of the present lifted jet flame cannot be represented by a single global stabilization point due to the presence of highly localized intermittent ignition phenomena occurring at the flame base. This is because the single global stabilization point migrates substantially in the spanwise direction, and frequently the migration from one location to another occurs over a very short interval of time ($\sim 0.04\tau_j$). The fast spanwise movement of the global stabilization point indicates that several independent ignition kernels or flame structures coexist near the flame base at any given time. Note that the integral length scale in the homogeneous direction, l_{33}, evaluated from an auto-correlation of the spanwise velocity, is approximately 0.3 mm at the flame base. Hence, there exist multiple flow structures in the spanwise direction which may modulate the local strain rate field. These flow structures contribute to the existence of multiple minima of the local stabilization point as shown in figure 2. From this perspective, it is clear that the definition of a global stabilization point is not able to capture the localized ignition processes.

Alternatively, a natural segmentation, which identifies neighborhoods around local maxima of a given scalar (e.g. OH or HO_2), are more suitable to track the centroid of a volumetric region representing an ignition kernel. Such a topological segmentation together with temporal tracking of multi-scale turbulent combustion data is a topic under current investigation (Mascarenhas *et al.* 2009). In the present study, however, it is

more feasible to segment the data into z–planes, and to track the movement of the local stabilization point within a given plane. We recognize that the local stabilization point in a given kernel, thus defined, may fluctuate in time, such that its centroid may shift to another spanwise location. However, one characteristic eddy time in the z-direction, $\tau_{33} = L_{33}/u_3'$, at the mean flame base is approximately $0.16\tau_j$ which is much shorter than one period of the stabilization point movement as will be discussed below. From the different time scales, we can assume that the effect of u_3' on the advection of a local stabilization point is insignificant. Therefore, the present planar segmentation, used in previous experiments (e.g. Upatnieks *et al.* 2004; Su *et al.* 2006), still provides useful correlation between key scalar and velocity fields at the local stabilization point. Henceforth, the stabilization point denotes the local stabilization point in a given z–plane, and not the global stabilization point.

First, we determine the statistical location of the stabilization point, obtained from the PDF shown in figure 15(a). To understand the mixing rate and ignition influence on the stabilization point, PDFs of ξ, χ, and Da are also presented in the figure. The PDF of the stabilization point varies over an axial distance of approximately $1.0H$ and transverse distance of approximately $0.5H$. The mean location of the stabilization point is at $x/H = 2.6$ and $y/H = -1.0$. The PDFs show that the most probable stabilization point lies at a mixture fraction slightly less than ξ_{MR} (≈ 0.05) with small χ and Da larger than unity. The corresponding $\overline{\xi}$, $\overline{\chi}$, and $\overline{Da}$ are approximately 0.033, 66 s^{-1}, and 20 respectively.

To further understand the fluctuations of the stabilization point, we examined the locus of the stabilization point for a given z–plane. Figure 16 shows the typical movement of the stabilization point for the $z = 0$ plane. It is readily observed that the locus forms a cycle of which period is approximately $2\tau_j$. To quantitatively evaluate the period in comparison

with characteristic turbulence time scales, the power spectrum of the stabilization point fluctuation ($h' = \overline{h} - h$) is evaluated using an FFT algorithm. Likewise, the power spectrum of the correlation function oscillations between axial velocity fluctuations on opposite sides of the jet is also calculated at $x = \overline{h}$. The correlation function, $R_u(\Delta y, \tau)$, is defined as:

$$R_u(\Delta y, \tau) = \overline{u_1'(x = \overline{h}, y = \delta_{1/2}, z, t) u_1'(x = \overline{h}, y = -\delta_{1/2}, z, t + \tau)}, \qquad (6.1)$$

such that the degree of correlation of axial velocity fluctuations over a transverse separation of $2\delta_{1/2}$ is a measure of the effects of the large-scale flow structure. The overbar in equation 6.1 denotes a time-average. The power spectrum evaluated at each z plane is averaged over the z-direction and then normalized by its maximum value. The result is presented in figure 17. It is readily observed that both power spectra exhibit a peak at a similar Strouhal number, $St = fH/U_j \sim 0.035$, corresponding to a time scale of approximately $2\tau_j$, which is similar to the period observed in figure 16. Note that, in addition to the first frequency peak, the correlation-function spectrum has two other peaks at $fH/U_j \sim 0.1$ and 0.2. Similar to the present result, three correlation-function frequencies in the near field of a planar non-reacting jet were also observed experimentally (e.g. Thomas & Goldschmidt 1986). From the dominant fluctuation frequencies of the spectra, the fluctuations of the stabilization point appear to be correlated with the passage of large-scale flow structures near the flame base although the time series from the DNS data may not be sufficiently long to provide a fully converged power spectrum.

Hammer & Roshko (2000) had also investigated the correlation between the large-scale jet time scale ($=2\delta_{1/2}/\widetilde{U}_0$), and the time scales of the fluctuations in the lift-off height from experiments in turbulent jet flames. Contrary to the present DNS results, they found that the dominant time scales of the stabilization point fluctuations were much longer, by over a factor of ten, than the large-scale jet time. They also did not observe any peak

in the power spectrum for the fluctuation of lift-off height. This apparent discrepancy may be due to their definition of St based on the large-scale jet time, which can be less than the correlation-function time scale by as much as a factor of ten in a round jet (e.g. Jung *et al.* 2004; Gamard *et al.* 2004). If St is defined based on the correlation-function frequency, then the measured stabilization point fluctuation time scale is comparable to the large-scale flow time scale, consistent with the present DNS results.

The stabilization point movement is further correlated with other key velocity and scalar quantities. Namely, the temporal evolution of the stabilization points along with flame-normal flow velocity ($-\mathbf{u}\cdot\mathbf{n}$), displacement speed ($S_d$) and its reaction and diffusion components (S_d^R and S_d^D), ξ, and χ at $z = 0$ plane are presented in figure 18. All values are evaluated at the stabilization point. The displacement speed of species k, S_d, is defined as:

$$S_d = S_d^R + S_d^D = \frac{1}{\rho|\boldsymbol{\nabla} Y_k|}\left(\dot{\omega}_k - \frac{\partial}{\partial x_j}(\rho Y_k V_{j,k})\right). \tag{6.2}$$

The iso-surface associated with the stabilization point, $Y_{\mathrm{OH}} = 0.001$, is used to evaluate the displacement speed. Equation 6.2 was first derived for non-reacting flows by Gibson (1968). It was then extended to reacting flows (e.g. Pope 1988; Poinsot *et al.* 1992; Ruetsch *et al.* 1995; Echekki & Chen 1999). S_d is evaluated rather than the density-weighted displacement speed, S_d^* ($\equiv \rho S_d/\rho_u$) because of the ambiguity in defining an appropriate upstream density, ρ_u in the turbulent flow. However, both the unweighted and weighted displacement speeds have similar values since ignition at the stabilization point occurs under nearly iso-thermal conditions, and thus, the density difference between the upstream flow and at the stabilization point is insignificant, whereas it is important in edge flames (e.g. Im & Chen 1999).

During the time period between $t/\tau_j = 8.8 \sim 9.6$, the stabilization point moves upstream and transversely inward as revealed from a comparison of figure 6 with figure 18.

The corresponding ξ is fuel-lean, close to ξ_{MR} (≈ 0.05), and the corresponding χ is relatively low. Therefore, the flame base is situated far from the jet core and the local conditions are favorable to auto-ignition. Consequently, the corresponding S_d is greater than the laminar flame speed by an order of magnitude, and also greater than the local flame-normal velocity. Hence, the stabilization point moves upstream and transversely inward following a large-scale flow structure. Note that a reference laminar flame speed at ξ_{MR} and 800 K, evaluated using PREMIX by Kee *et al.* (1985), is approximately 2.6 m s^{-1}. The actual laminar flame speed is undefined at the stabilization point since the mixture is reactive; however, the speed at 800 K is intended to provide an estimate by which to compare the displacement speed of the stabilization point.

By subsequently migrating transversely inward towards relatively fuel-rich regions, the stabilization point encounters a jet structure with high convective velocities and high χ during the time period between $t/\tau_j = 9.6 \sim 10.8$. Under these conditions, auto-ignition near ξ_{MR} is retarded and the displacement speed at the stabilization point decreases, and even becomes negative, for example at $t/\tau_j \sim 10.2$ and 10.4, due to small S_d^R and large negative S_d^D. This results in a rapid movement of the stabilization point downstream and transversely outward. Subsequently, the stabilization point returns to its original point, forming a complete cycle as shown in figure 16. Occasionally, a negative displacement speed at the leading edge of a hydrogen/air non-premixed flame can occur where the flame is locally quenched by high scalar dissipation rate (e.g. Yoo & Im 2005). Under the present conditions, the downstream movement of the stabilization point is primarily attributed to large local convective velocity, and intermittently, negative displacement speed associated with quenching from locally high mixing rates.

From these observations, we postulate a stabilization mechanism, incorporating the concept of large-scale flow structure proposed by Su *et al.* (2006), such that the flame

base fluctuates with the passage of a series of large-scale flow mixing structures and auto-ignition in fuel-lean mixtures. As illustrated in the schematic in figure 19, after auto-ignition occurs in fuel-lean mixtures with low χ, the stabilization point moves upstream, following a large-scale flow structure and tracking the lean flammable mixture which lies outside of the core jet region. After the stabilization point reaches its minimum axial location that is close to the core jet, the stabilization point starts to move downstream again as it encounters another large-scale flow structure with high axial jet velocity and scalar dissipation rate, thus completing a full cycle. A comparison of figures 6 and 18 readily shows one cycle of the flame base movement, consistent with this hypothesis.

The findings of the present study suggest that turbulent lifted jet flames in heated coflow stabilize through a competition between convection/extinction by high axial velocity and high scalar dissipation rate, and auto-ignition/flame propagation, depending on the coflow temperature and the stabilization point location relative to the core jet. When the coflow temperature is relatively low but high enough to support auto-ignition in fuel-lean mixtures, auto-ignition first occurs far downstream of a final stabilization location and subsequently, the flame base propagates upstream by spontaneous ignition or flame propagation. Ultimately, however, the flame base stabilizes by the flame propagation mechanism, and not by auto-ignition, due to the relatively long ignition delay. On the contrary, when the coflow temperature is much higher than the cross-over temperature, auto-ignition becomes the dominant stabilization mechanism because the spontaneous ignition propagation is much greater than deflagration flame propagation. In either case, however, a high coflow temperature provides favorable conditions for stabilizing a lifted flame base. The conditions of the present study correspond to the latter case such that auto-ignition is the dominant stabilization mechanism.

7. Conclusions

Three-dimensional direct numerical simulation of a turbulent lifted hydrogen/air slot-burner jet flame in an auto-ignitive heated coflow was performed using detailed chemistry and mixture-averaged transport properties. The results show that, given a high coflow temperature, auto-ignition is the key mechanism responsible for flame stabilization, and HO_2 is important in initiating auto-ignition upstream of the flame base. Nominally, auto-ignition is found to occur in hot, fuel-lean regions. Several independent measures – Damköhler number, the spatial structure of the intermediate species, and the elementary reaction flux analysis – all clearly demonstrate the presence of auto-ignition at the flame base. In particular, large values of Da near the flame base, the existence of HO_2 upstream of high-temperature radicals (O, OH, and H), and the balance of R11 ($HO_2 + H \rightarrow OH + OH$) and R9 ($H + O_2 + M \rightarrow HO_2 + M$) at the flame base are all hallmarks of auto-ignition.

The conditional mean of the scalar dissipation rate is found to be an order of magnitude smaller than the laminar extinction scalar dissipation rate at the flame base, and larger than the laminar ignition scalar dissipation rate. However, the fluctuation of scalar dissipation rate is comparable to its mean value. Therefore, auto-ignition can occur in mixtures where the local scalar dissipation rate remains below the laminar ignition scalar dissipation rate long enough. The high probability of the occurrence of auto-ignition at the flame base is confirmed by the PDFs of scalar dissipation rate and Damköhler number, indicating that mean scalar dissipation rate is lower than the laminar ignition scalar dissipation rate and Damköhler number is larger than unity. Lagrangian statistics provided by particle tracking in the DNS in the future will provide the cumulative time history of scalar dissipation rate encountered by a given ignition kernel which may be useful for unsteady flamelet models.

From the statistics of the flame index and Damköhler number at the flame base, it is found that ignition under the opposed mixing mode prevails for the present conditions, and hence, most of the heat release is generated from the opposed mixing mode. Further downstream, bimodal combustion is observed with the coexistence of both rich premixed and non-premixed flames as well as auto-ignition.

It is also found that the stabilization points form a cycle with the passage of large-scale flow structure, and the flame stabilization is determined by the balance between the local axial velocity and auto-ignition which favors hot environments with low scalar dissipation rate.

The work at Sandia National Laboratories (SNL) was supported by the Division of Chemical Sciences, Geosciences, and Biosciences, Office of Basic Energy Sciences of the U. S. Department of Energy, and the U. S. Department of Energy SciDAC Program. SNL is a multiprogram laboratory operated by Sandia Corporation, a Lockheed Martin Company, for the U. S. Department of Energy under contract DE-AC04-94AL85000. The work at Oak Ridge National Laboratory (ORNL) was supported by and this research used resources of the National Center for Computational Sciences (NCCS) at ORNL, which is supported by the Office of Science of the U.S. DOE under contract DE-AC05-00OR22725.

REFERENCES

Bilger, R. W. 1979 Turbulent flows with nonpremixed reactants. In *Turbulent reacting flows* (ed. P. A. Libby & F. A. Williams), *Topics in Applied Physics*, vol. 44, pp. 65–113. Springer-Verlag.

Bilger, R. W. 1988 The structure of turbulent nonpremixed flames. *Proc. Combust. Inst.* **22**, 475–488.

Borghi, R. 1988 Turbulent combustion modelling. *Prog. Energy Combust. Sci.* **14**, 245–292.

Buckmaster, J. 2002 Edge flames. *Prog. Energy Combust. Sci.* **28**, 435–475.

Cabra, R., Myhrvold, T., Chen, J. Y., Dibble, R. W., Karpetis, A. N. & Barlow, R. S. 2002 Simultaneous laser Raman-Rayleigh-LIF measurements and numerical modeling results of a lifted turbulent H_2/N_2 jet flame in a vitiated coflow. *Proc. Combust. Inst.* **29**, 1881–1888.

Cao, R. R., Pope, S. B. & Masri, A. R. 2005 Turbulent lifted flames in a vitiated coflow investigated using joint PDF calculations. *Combust. Flame* **142**, 438–453.

Chen, J. H., Choudhary, A., de Supinski, B., DeVries, M., Hawkes, E. R., Klasky, S., Liao, W. K., Ma, K. L., Mellor-Crummey, J., Podhorszki, N., Sankaran, R., Shende, S. & Yoo, C. S. 2009 Terascale direct numerical simulations of turbulent combustion using S3D. *Comput. Sci. Disc.* **2**, 015001.

Choi, C. W. & Puri, I. K. 2000 Flame stretch effects on partially premixed flames. *Combust. Flame* **123**, 119–139.

Chung, S. H. 2007 Stabilization, propagation and instability of tribrachial triple flame. *Proc. Combust. Inst.* **31**, 877–892.

Dec, J. E. 1997 Conceptual model of Di Diesel combustion based on laser-sheet imaging. *SAE Trans.* **105**, 1319–1348.

Domingo, P., Vervisch, L. & Rveillon, J. 2005 DNS analysis of partially premixed combustion in spray and gaseous turbulent flame-bases stabilized in hot air. *Combust. Flame* **152**, 415–432.

Domingo, P., Vervisch, L. & Veynante, D. 2008 Large-eddy simulation of a lifted methane jet flame in a vitiated coflow. *Combust. Flame* **140**, 172–195.

Echekki, T. & Chen, J. H. 1999 Analysis of the contribution of curvature to premixed flame propagation. *Combust. Flame* **118**, 308–311.

Echekki, T. & Chen, J. H. 2003 Direct numerical simulation of autoignition in non-homogeneous hydrogen-air mixtures. *Combust. Flame* **134**, 169–191.

Eswaran, V. & Pope, S. B. 1988 Direct numerical simulations of the turbulent mixing of a passive scalar. *Phys. Fluids* **31**, 506–520.

Gamard, S., Jung, D. & George, W. K. 2004 Downstream evolution of the most energetic

modes in a turbulent axisymmetric jet at high Reynolds number. Part 2. The far-field region. *J. Fluid Mech.* **514**, 205–230.

Gibson, C. H. 1968 Fine structure of scalar fields mixed by turbulence. I. Zero-gradient points and minimal gradient surfaces. *Phys. Fluids* **11**, 2305–2315.

Gkagkas, K. & Lindstedt, R. P. 2006 PDF modeling of hydrogen/air lifted flame. In *8^{th} International workshop on measurement and computation of turbulent nonpremixed flames, Heigelberg, Germany*.

Gordon, R. L., Masri, A. R. & Mastorakos, E. 2008 Simultaneous Rayleigh temperature, OH- and CH_2O-LIF imaging of methane jets in a vitiated coflow. *Combust. Flame* **155**, 181–195.

Gordon, R. L., Masri, A. R., Pope, S. B. & Goldin, G. M. 2007 A numerical study of auto-ignition in turbulent lifted flames issuing into a vitiated co-flow. *Combust. Theory Modelling* **11**, 351–376.

Hammer, J. A. & Roshko, A. 2000 Temporal behavior of lifted turbulent jet flames. *Combust. Sci. Technol.* **155**, 75–103.

Helenbrook, B. T., Im, H. G. & Law, C. K. 1998 Theory of radical-induced ignition of counterflowing hydrogen versus oxygen at high temperature. *Combust. Flame* **112**, 242–252.

Im, H. G. & Chen, J. H. 1999 Structure and propagation of triple flames in partially premixed hydrogen-air mixtures. *Combust. Flame* **119**, 436–454.

Im, H. G., Chen, J. H. & Law, C. K. 1998 Ignition of hydrogen-air mixing layer in turbulent flows. *Proc. Combust. Inst.* **27**, 1047–1056.

Jiménez, C. & Cuenot, B. 2007 DNS study of stabilization of turbulent triple flames by hot gases. *Proc. Combust. Inst.* **31**, 1649–1656.

Joedicke, A., Peters, N. & Mansour, M. 2005 The stabilization mechanism and structure of turbulent hydrocarbon lifted flames. *Proc. Combust. Inst.* **30**, 901–909.

Jones, W. P. & Navarro-Martinez, S. 2007 Large eddy simulation of autoignition with a subgrid probability density function method. *Combust. Flame* **150**, 170–187.

Jung, D., Gamard, S. & George, W. K. 2004 Downstream evolution of the most energetic

modes in a turbulent axisymmetric jet at high Reynolds number. Part 1. The near-field region. *J. Fluid Mech.* **514**, 173–204.

Kalghatgi, G. T. 1984 Lift-off heights and visible lengths of vertical turbulent jet diffusion flames in still air. *Combust. Sci. Tech.* **41**, 17–29.

Kee, R. J., Dixon-Lewis, G., Warnatz, J., Coltrin, M. E. & Miller, J. A. 1986 A fortran computer code package for the evaluation of gas-phase multicomponent transport properties. *Tech. Rep.* SAND86-8246. Sandia National Labs.

Kee, R. J., Grcar, J. F., Smooke, M. D. & Miller, J. A. 1985 A fortran program for modeling steady laminar one-dimensional flames. *Tech. Rep.* SAND85-8240. Sandia National Labs.

Kee, R. J., Rupley, F. M., Meeks, E. & Miller, J. A. 1996 CHEMKIN-III: A fortran chemical kinetic package for the anaylsis of gas-phase chemical and plasma knietics. *Tech. Rep.* SAND96-8216. Sandia National Labs.

Kennedy, C. A. & Carpenter, M. H. 1994 Several new numerical methods for compressible shear-layer simulations. *Appl. Num. Math.* **14**, 397–433.

Kennedy, C. A., Carpenter, M. H. & Lewis, R. M. 2000 Low-storage, explicit Runge–Kutta schemes for the compressible Navier–Stokes equations. *Appl. Num. Math.* **35**, 117–219.

Kreutz, T. G. & Law, C. K. 1996 Ignition in nonpremixed counterflowing hydrogen versus heated air: computational study with detailed chemistry. *Combust. Flame* **104**, 157–175.

Law, C. K. 2006 *Combustion physics*. Cambridge University Press.

Li, J., Zhao, Z., Kazakov, A. & Dryer, F. L. 2004 An updated comprehensive kinetic model of hydrogen combustion. *Int. J. Chem. Kinet.* **36**, 566–575.

Lutz, A. E., Kee, R. J., Grcar, J. F. & Rupley, F. M. 1997 A fortran program for computing opposed-flow diffusion flames. *Tech. Rep.* SAND96-8243. Sandia National Labs.

Lyons, K. M. 2007 Toward an understanding of the stabilization mechanisms of lifted turbulent jet flames: experiments. *Prog. Energy Combust. Sci.* **33**, 211–231.

Markides, C. N. & Mastorakos, E. 2005 An experimental study of hydrogen autoignition in a turbulent co-flow of heated air. *Proc. Combust. Inst.* **30**, 883–891.

Mascarenhas, A., Grout, R.W., Bremer, P.-T., Pascucci, V., Hawkes, E. & Chen, J.H.

2009 Topological feature extraction for comparison of length scales in terascale combustion simulation data. In *Topoinvis'09: Topological Methods in Data Analysis and Visualization*. Springer-Verlag.

Masri, A. R., Cao, R., Pope, S. B. & Goldin, G. M 2004 PDF calculations of turbulent lifted flames of H_2/N_2 fuel issuing into a vitiated co-flow. *Combust. Theory Modelling* **8**, 1–22.

Mastorakos, E., Baritaud, T. A. & Poinsot, T. J. 1997*a* Numerical simulations of autoignition in turbulent mixing flows. *Combust. Flame* **109**, 198–223.

Mastorakos, E., Cruz, A. Pires Da & Poinsot, T. J. 1997*b* A model for the effects of mixing on the autoignition of turbulent flows. *Combust. Sci. Tech.* **125**, 243–282.

Miake-Lye, R. C. & Hammer, J. A. 1988 Alifted turbulent jet flames: a stability criterion based on the jet large-scale structure. *Proc. Combust. Inst.* **22**, 817–824.

Mizobuchi, Y., Tachibana, S., Shinio, J., Ogawa, S. & Takeno, T. 2002 A numerical analysis of the structure of a turbulent hydrogen jet lifted flame. *Proc. Combust. Inst.* **29**, 2009–2015.

Mueller, C. J., Driscoll, J. F., Reuss, D. L., Drake, M. C. & Roslik, M. E. 1998 Vorticity generation and attenuation as vortices convect through a premixed flame. *Combust. Flame* **112**, 342–358.

Muñiz, L. & Mungal, M. G. 1997 Instantaneous flame-stabilization velocities in lifted-jet diffusion flames. *Combust. Flame* **111**, 16–31.

Peters, N. 2000 *Turbulent combustion*. Cambridge University Press.

Peters, N. & Williams, F. A. 1983 Liftoff characteristics of turbulent jet diffusion flames. *AIAA J.* **21**, 423–429.

Pickett, L. M. 2005 Low flame temperature limits for mixing-controlled Diesel combustion. *Proc. Combust. Inst.* **30**, 2727–2735.

Pickett, L. M., Siebers, D. L. & Idicheria, C. A. 2005 Relationship between ignition processes and the lift-off length of Diesel fuel jets. *SAE paper 2005–01–3843* .

Pitts, W. M. 1998 Assessment of theories for the behavior and blowout of lifted turbulent jet diffusion flame. *Proc. Combust. Inst.* **22**, 809–816.

Poinsot, T. J., Echekki, T. & Mungal, M. G. 1992 A study of the laminar flame tip and implications for premixed turbulent combustion. *Combust. Sci. Technol.* **81**, 45–73.

Poinsot, T. J. & Lele, S. K. 1992 Boundary conditions for direct numerical simulations of compressible viscous flows. *J. Comput. Phys.* **101**, 104–139.

Pope, S. B. 1988 The evolution of surfaces in turbulence. *Int. J. Eng. Sci.* **26**, 445–469.

Pope, S. B. 2000 *Turbulent flows*. Cambridge University Press.

Richardson, E. S., Yoo, C. S. & Chen, J. H. 2009 Analysis of second-order conditional moment closure applied to an autoignitive lifted hydrogen jet flame. *Proc. Combust. Inst.* **32**, 1695–1703.

Ruetsch, G. R., Vervisch, L. & Liñán, A. 1995 Effects of heat release on triple flames. *Phys. Fluids* **7**, 1447–1454.

Sankaran, R., Hawkes, E. R., Chen, J. H., Lu, T. & Law, C. K. 2007 Structure of a spatially developing turbulent lean methane-air bunsen flame. *Proc. Combust. Inst.* **31**, 1291–1298.

Schefer, R. W. & Goix, P. J. 1998 Mechanism of flame stabilization in turbulent lifted-jet flames. *Combust. Flame* **112**, 559–574.

Stanley, S. A., Sarkar, S. & Mellado, J. P. 2002 A study of the flow-field evolution and mixing in a planar turbulent jet using direct numerical simulation. *J. Fluid Mech.* **450**, 377–407.

Su, L. K. & Clemens, N. T. 2003 The structure of fine-scale scalar mixing in gas-phase planar turbulent jets. *J. Fluid Mech.* **488**, 1–29.

Su, L. K., Sun, O. S. & Mungal, M. G. 2006 Experimental investigation of stabilization mechanisms in turbulent, lifted jet diffusion flames. *Combust. Flame* **144**, 494–512.

Sutherland, J. C. & Kennedy, C. A. 2003 Improved boundary conditions for viscous, reacting, compressible flows. *J. Comput. Phys.* **191**, 502–524.

Tacke, M. M., Geyer, D., Hassel, E. P. & Janicka, J. 1998 A detailed investigation of the stabilization point of lifted turbulent diffusion flames. *Proc. Combust. Inst.* **27**, 1157–1165.

Thomas, F. O. & Goldschmidt, V. W. 1986 Structural characteristics of a developing turbulent planar jet. *J. Fluid. Mech.* **163**, 227–256.

Upatnieks, A., Driscoll, J. F., Rasmussen, C. C. & Ceccio, S. L. 2004 Liftoff of turbulent jet flames–assessment of edge flame and other concepts using cinema-PIV. *Combust. Flame* **138**, 259–272.

Vanquickenborne, L. & van Tiggelen, A. 1966 The stabilization mechanism of lifted diffusion flames. *Combust. Flame* **10**, 59–69.

Yamashita, H., Shimada, M. & Takeno, T. 1996 A numerical study on flame stability at the transition point of jet diffusion flames. *Proc. Combust. Inst.* **26**, 27–34.

Yeung, P. K. & Pope, S. B. 1989 Lagrangian statistics from direct numerical simulations of isotropic turbulence. *J. Fluid Mech.* **207**, 531–586.

Yoo, C. S. & Im, H. G. 2005 Transient dynamics of edge flames in a laminar nonpremixed hydrogen-air counterflow. *Proc. Combust. Inst.* **20**, 349–356.

Yoo, C. S. & Im, H. G. 2007 Characteristic boundary conditions for simulations of compressible reacting flows with multi-dimensional, viscous and reaction effects. *Combust. Theory Modelling* **11**, 259–286.

Yoo, C. S., Wang, Y., Trouvé, A. & Im, H. G. 2005 Characteristic boundary conditions for direct numerical simulations of turbulent counterflow flames. *Combust. Theory Modelling* **9**, 617–646.

Zeldovich, Y. B. 1980 Regime classification of an exothermic reaction with nonuniform initial conditions. *Combust. Flame* **39**, 211–214.

Parameter	
Jet width(H)	1.92 mm
Fuel width(H_ξ)	1.60 mm
Domain size ($L_x \times L_y \times L_z$)	$12.5H \times 16.7H \times 3.3H$
Number of grid points ($N_x \times N_y \times N_z$)	$1600 \times 1372 \times 430$
Mean inlet jet velocity (U_j)	347 m s^{-1}
Laminar coflow velocity (U_c)	4 m s^{-1}
Jet temperature (T_j)	400 K
Laminar coflow temperature (T_c)	1100 K
Jet Reynolds number ($\mathrm{Re}_j = U_j H/\nu$)	11 000
Velocity fluctuation† (u'/U_j)	0.091
Turbulence length scale‡ (l_t/H)	0.77
Integral length scale¶ (l_{33}/H)	0.37
Turbulence Reynolds number ($\mathrm{Re}_t = u' l_{33}/\nu$)	340

† u', l_t, and l_{33} are evaluated at the 1/4th streamwise location along the jet centerline

‡ Turbulent length scale, l_t is estimated as $l_t = \widetilde{k}^{3/2}/\widetilde{\epsilon}$ where $\widetilde{k}$ and $\widetilde{\epsilon}$ are the Favre averaged turbulent kinetic energy and dissipation rate, respectively.

¶ Integral length scale, l_{33} is defined as the integral of the auto-correlation of spanwise component of velocity in the spanwise direction

Table 1: Numerical and physical parameters of the DNS

	Reaction		A [cm,mol,s]	n	E [kcal mol^{-1}]
R1.	$H + O_2 \leftrightarrow O + OH$		3.55×10^{15}	-0.41	16.6
R2.	$O + H_2 \leftrightarrow OH + H$		5.08×10^{4}	2.67	6.29
R3.	$H_2 + OH \leftrightarrow H_2O + H$		2.16×10^{8}	1.51	3.43
R4.	$O + H_2O \leftrightarrow OH + OH$		2.97×10^{6}	2.02	13.4
R5.	$H_2 + M \leftrightarrow H + H + M$†		4.58×10^{19}	-1.40	104.38
R6.	$O + O + M \leftrightarrow O_2 + M$†		6.16×10^{15}	-0.50	0.00
R7.	$O + H + M \leftrightarrow OH + M$†		4.71×10^{18}	-1.0	0.00
R8.	$H + OH + M \leftrightarrow H_2O + M$†		3.8×10^{22}	-2.00	0.00
R9.	$H + O_2 + M \leftrightarrow HO_2 + M$‡	k_0	6.37×10^{20}	-1.72	0.52
		k_∞	1.48×10^{12}	0.60	0.00
R10.	$HO_2 + H \leftrightarrow H_2 + O_2$		1.66×10^{13}	0.00	0.82
R11.	$HO_2 + H \leftrightarrow OH + OH$		7.08×10^{13}	0.00	0.30
R12.	$HO_2 + O \leftrightarrow OH + O_2$		3.25×10^{13}	0.00	0.00
R13.	$HO_2 + OH \leftrightarrow H_2O + O_2$		2.89×10^{13}	0.00	-0.50
R14.	$HO_2 + HO_2 \leftrightarrow H_2O_2 + O_2$¶		4.20×10^{14}	0.00	11.98
	$HO_2 + HO_2 \leftrightarrow H_2O_2 + O_2$		1.30×10^{11}	0.00	-1.63
R15.	$H_2O_2 + M \leftrightarrow OH + OH + M$‖	k_0	1.20×10^{17}	0.00	45.5
		k_∞	2.95×10^{14}	0.00	48.4
R16.	$H_2O_2 + H \leftrightarrow H_2O + OH$		2.41×10^{13}	0.00	3.97
R17.	$H_2O_2 + H \leftrightarrow HO_2 + H_2$		4.82×10^{13}	0.00	7.95
R18.	$H_2O_2 + O \leftrightarrow OH + HO_2$		9.55×10^{6}	2.00	3.97
R19.	$H_2O_2 + OH \leftrightarrow HO_2 + H_2O$¶		1.00×10^{12}	0.00	0.00
	$H_2O_2 + OH \leftrightarrow HO_2 + H_2O$		5.80×10^{14}	0.00	9.56

† Efficiency factors are $\epsilon_{H_2O} = 12.0$ and $\epsilon_{H_2} = 2.5$

‡ Troe parameter is $F_c = 0.8$. Efficiency factors are $\epsilon_{H_2O} = 11.0$, $\epsilon_{H_2} = 2.0$, and $\epsilon_{O_2} = 0.78$

¶ R14 and R19 are expressed as the sum of the two rate expressions.

‖ Troe parameter is $F_c = 0.5$. Efficiency factors are $\epsilon_{H_2O} = 12.0$ and $\epsilon_{H_2} = 2.5$

Table 2: Elementary $H_2/O_2/N_2$ reactions ($k = AT^n \exp(-E/RT)$ from Li *et al.* 2004)

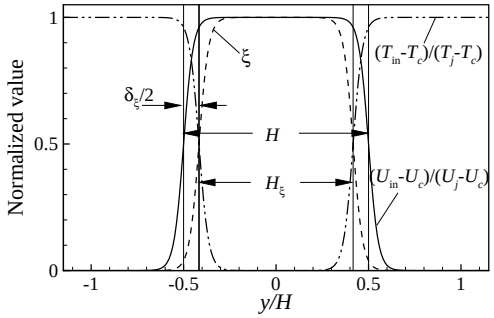

Figure 1: Mean profiles at the inlet boundary

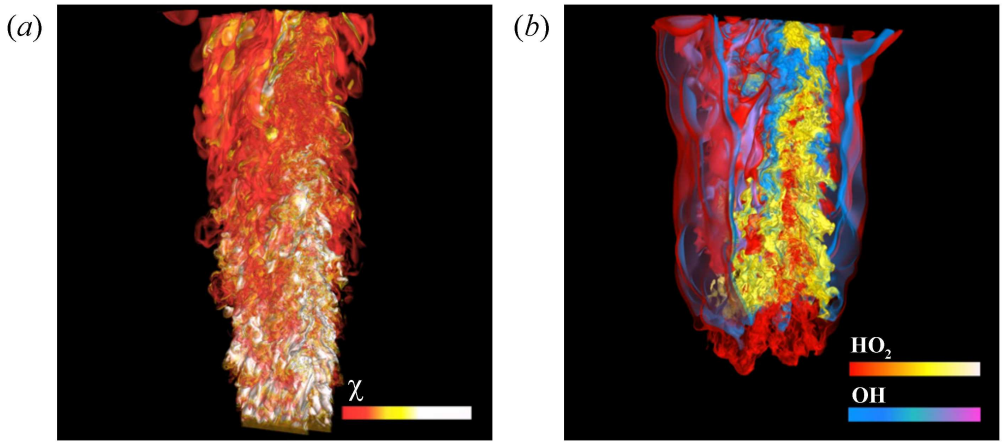

Figure 2: Instantaneous images of (a) logarithm of scalar dissipation rate, and (b) mass fractions of HO_2 and OH

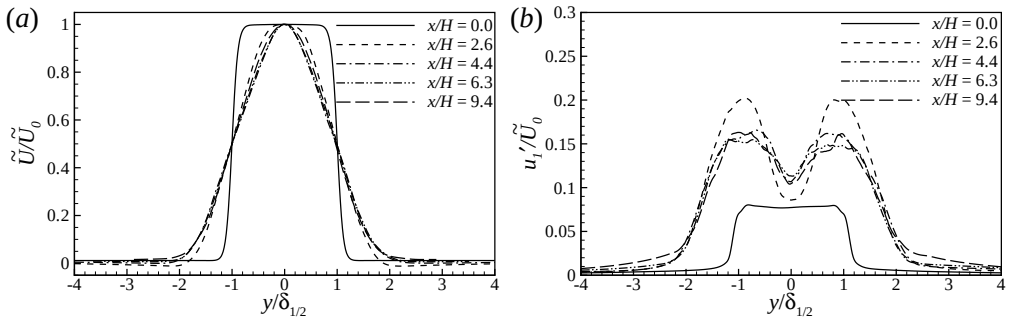

Figure 3: Axial variation of (a) mean axial velocity, $(\widetilde{U})$ and (b)velocity fluctuation,(u_1').

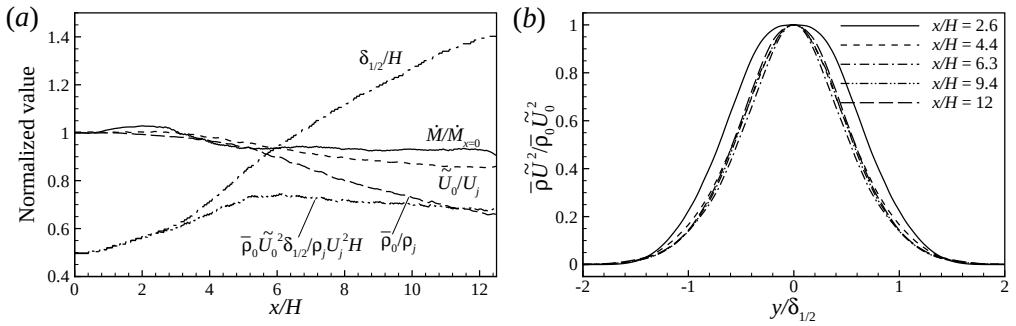

Figure 4: (a) Axial evolution of the mean axial velocity at the centerline, $\widetilde{U}_0$, the jet half-width, $\delta_{1/2}$, the mean density at the centerline, $\overline{\rho}_0$, $\overline{\rho}_0\widetilde{U}_0^2\delta_{1/2}$, and $\dot{M}$, and (b) axial variation of $\overline{\rho}\widetilde{U}^2$, where U_j and ρ_j denote the mean axial velocity and density of the fuel jet at the inlet, respectively.

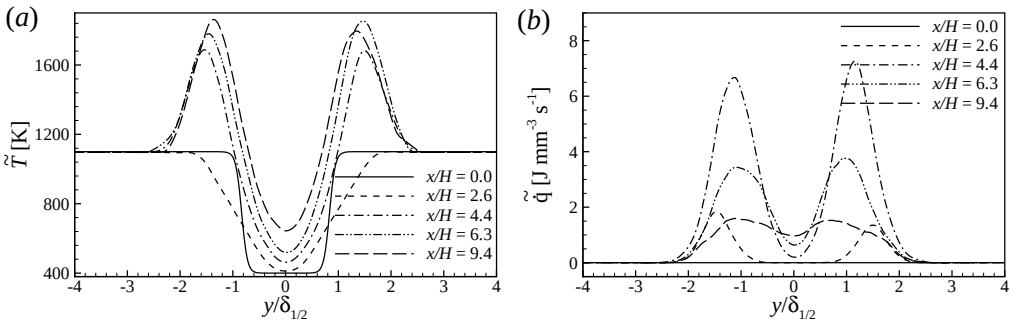

Figure 5: Axial variation of (a) mean temperature ($\widetilde{T}$) and (b) heat release rate ($\widetilde{\dot{q}}$).

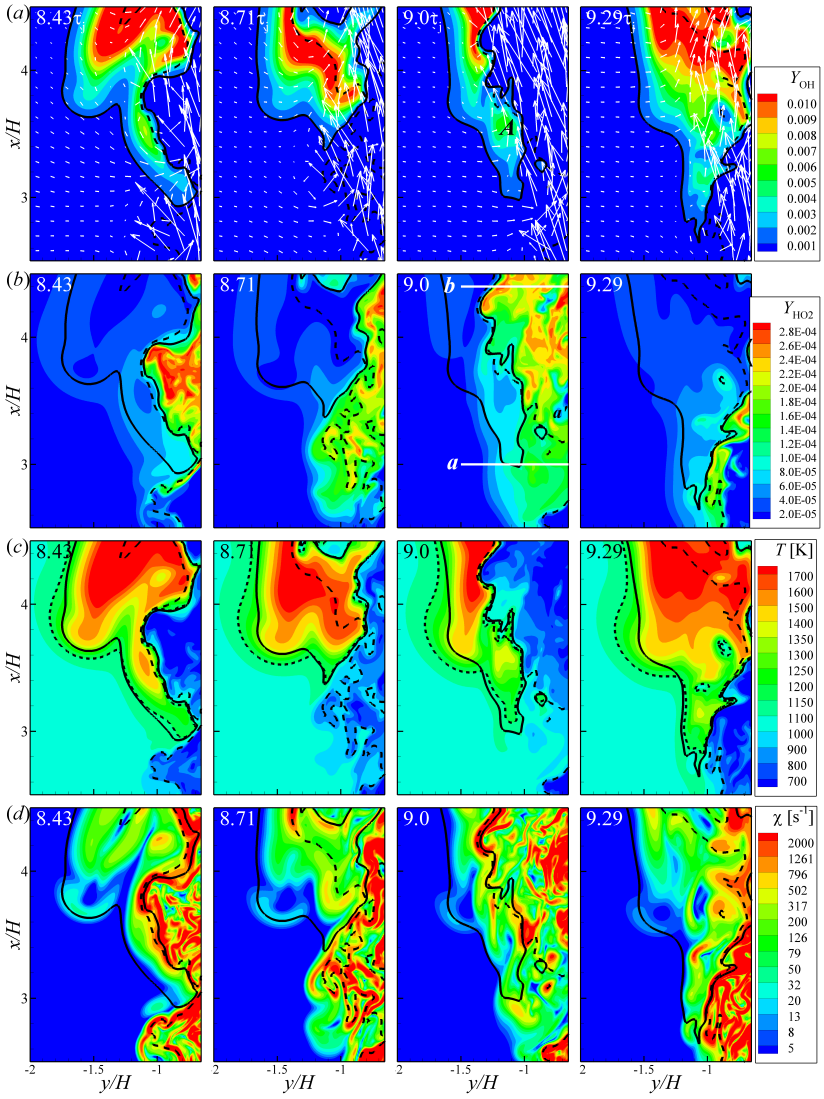

Figure 6: Sequential images of (a) Y_{OH}, (b) Y_{HO_2}, (c) temperature, and (d) scalar dissipation rate isocontours (flood) at the leading edge on the left branch of the lifted flame with velocity field (arrowed line) from $t/\tau_j = 8.43$ to 9.29 at $z = 0$. Solid and dashed lines denote $Y_{\mathrm{OH}} = 0.001$ and ξ_{st} isolines, respectively. Dotted lines in (c) represent $T = 1150$ K isolines.

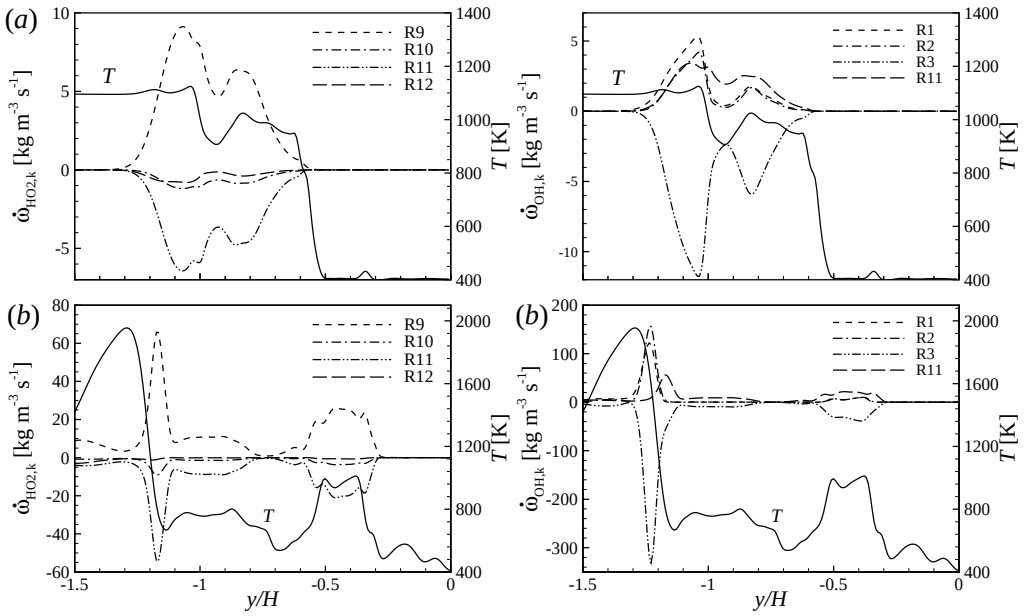

Figure 7: Profiles of the elementary reaction rates of HO_2 (left) and OH (right), and temperature at (a) $x/H = 3.0$ ('a' cut in figure 6) and (b) $x/H = 4.4$ ('b' cut in figure 6) at $z = 0$ and $t/\tau_j = 9$ along the left branch of the lifted flame.

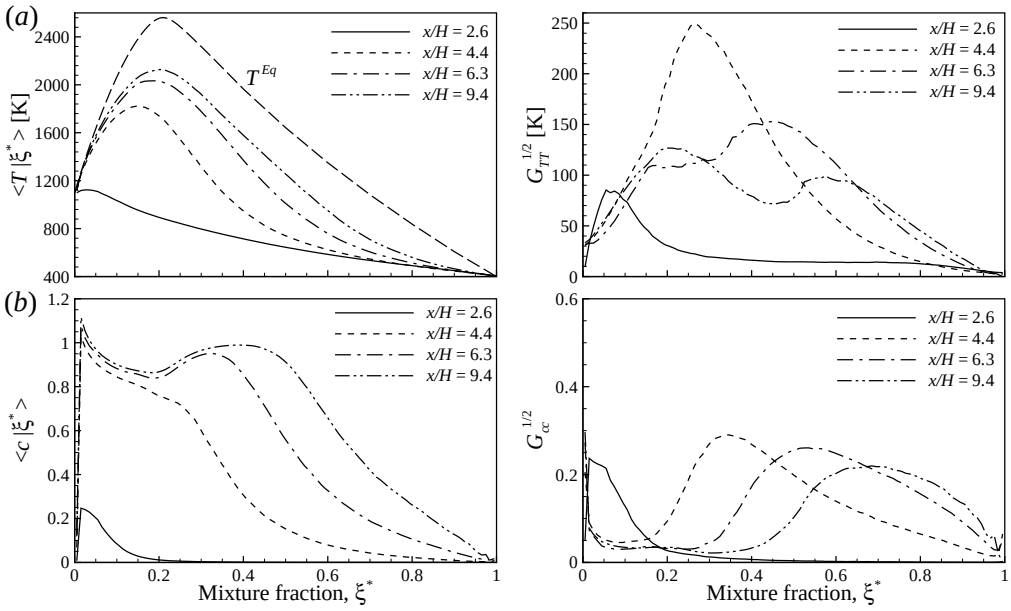

Figure 8: Axial variation of conditional Favre mean (left) and r.m.s. (right) of (a) temperature, and (b) progress variable. T^{Eq} denotes the equilibrium temperature profile.

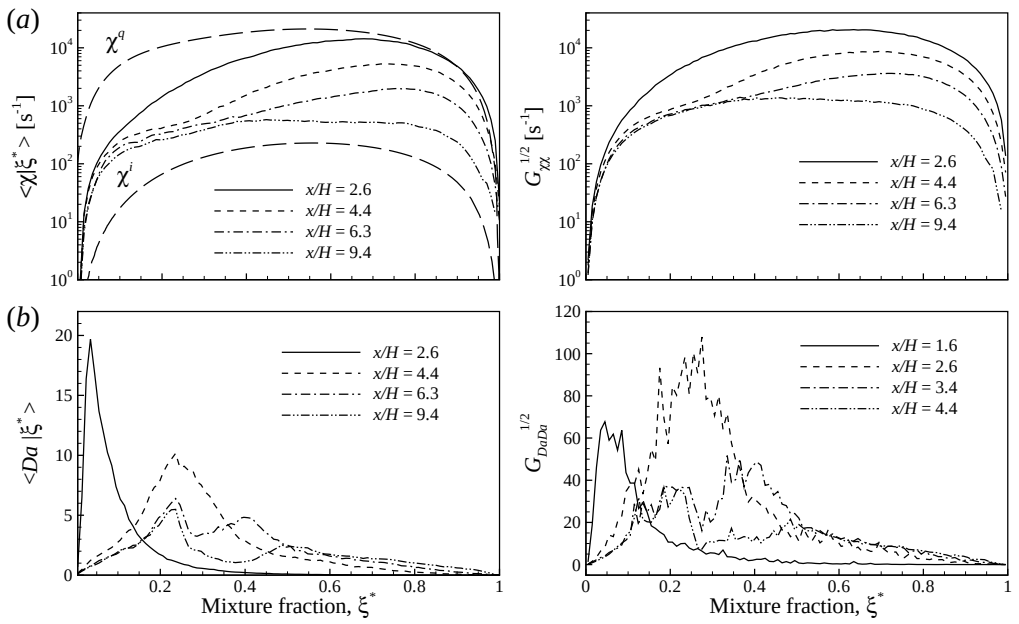

Figure 9: Axial variation of conditional Favre means (left) and r.m.s. (right) for (a) scalar dissipation rate and (b) Damköhler number. χ^q and χ^i denote the laminar extinction and ignition scalar dissipation rates, respectively.

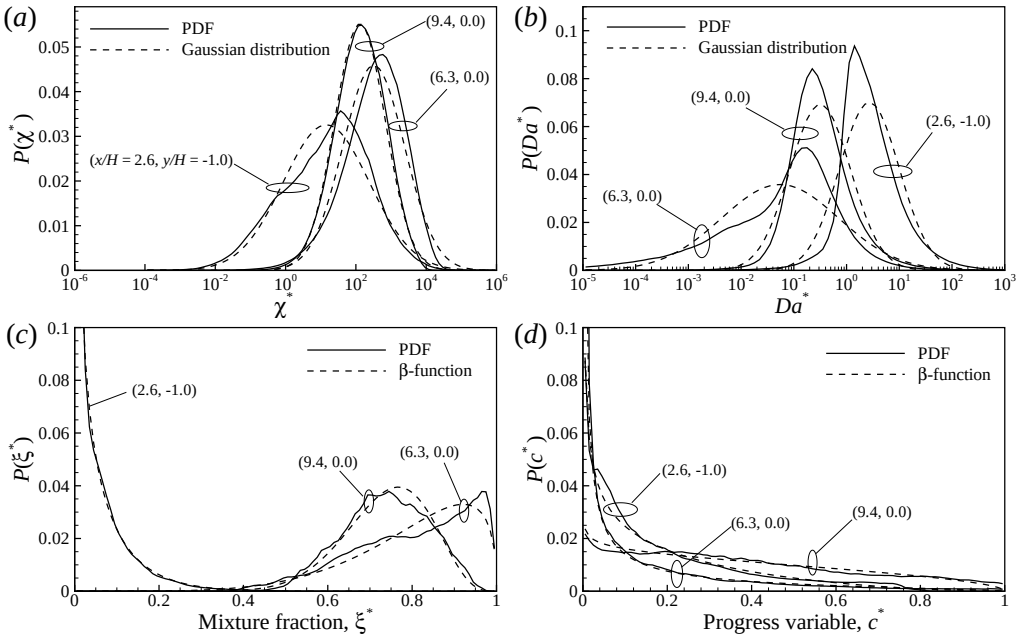

Figure 10: PDF of (a) scalar dissipation rate, (b) Damköhler number, (c) mixture fraction, and (d) progress variable at different locations. Dashed lines represent Gaussian distributions and β-functions which are evaluated using the first-two moments from DNS data. The values in the parenthesis denote x and y positions.

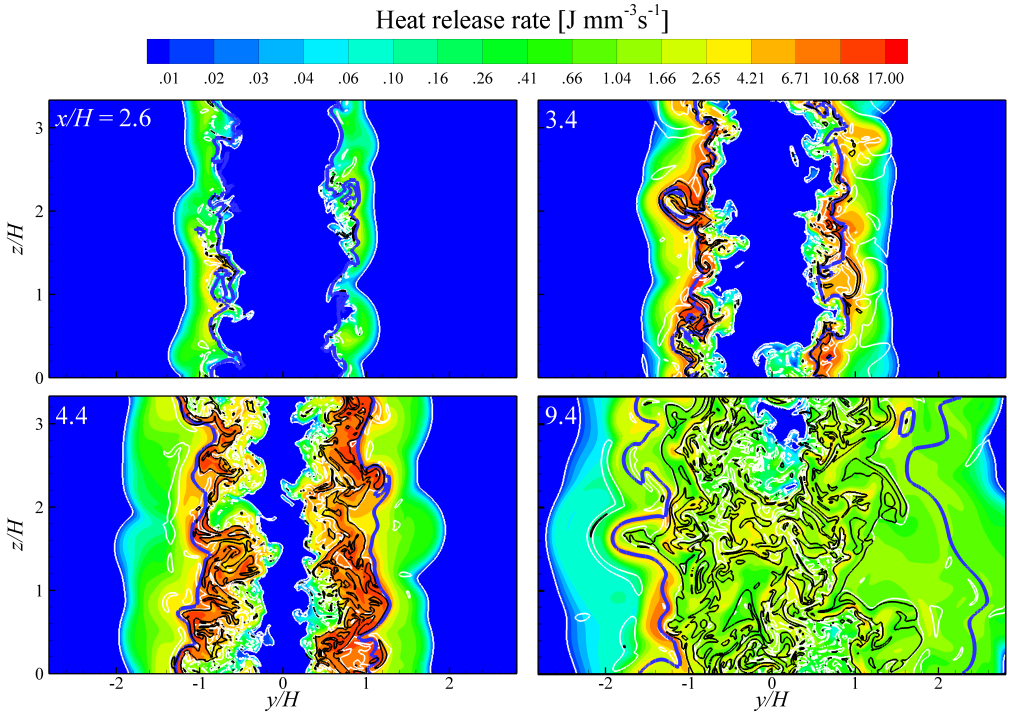

Figure 11: Isocontours of heat release rate with ξ_{st} isoline (blue line) for different axial locations at $t/\tau_j = 9$. The white and black lines represent the flame index value of -0.707 and 0.707, which represent opposed and aligned mixing modes, respectively.

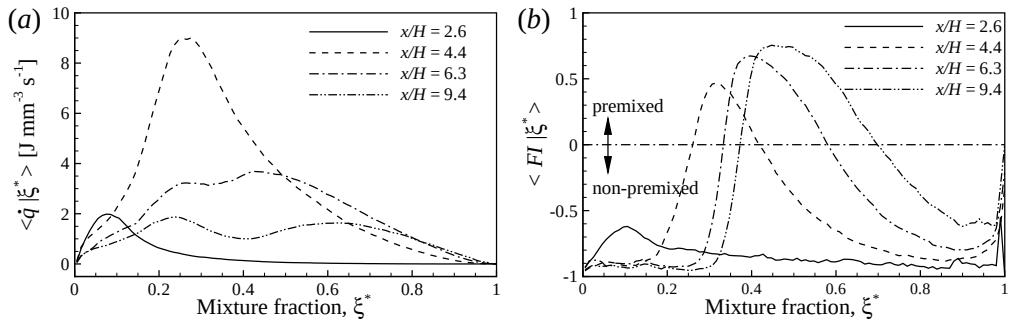

Figure 12: Axial variation of the conditional Favre means for (a) heat release rate and (b) flame index with a cutoff value of $\dot{q} = 0.01$ J mm^{-3}s^{-1}.

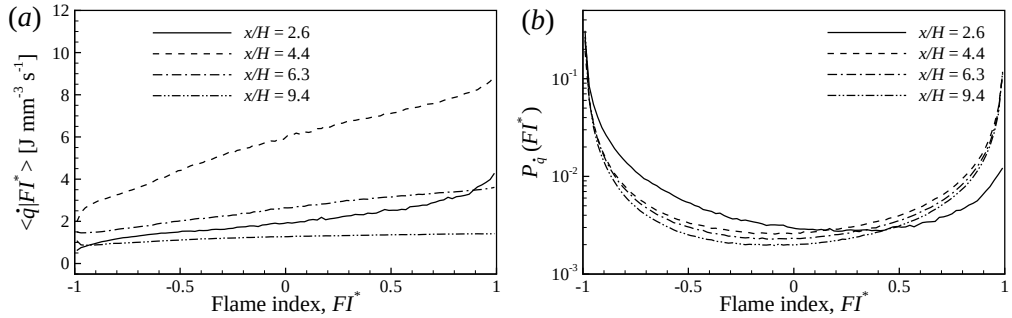

Figure 13: Axial variation of (a) mean heat release rate conditional on $FI = FI^*$ and (b) heat release rate-weighted PDF of FI with a cutoff value of $\dot{q} = 0.01$ J mm^{-3}s^{-1}.

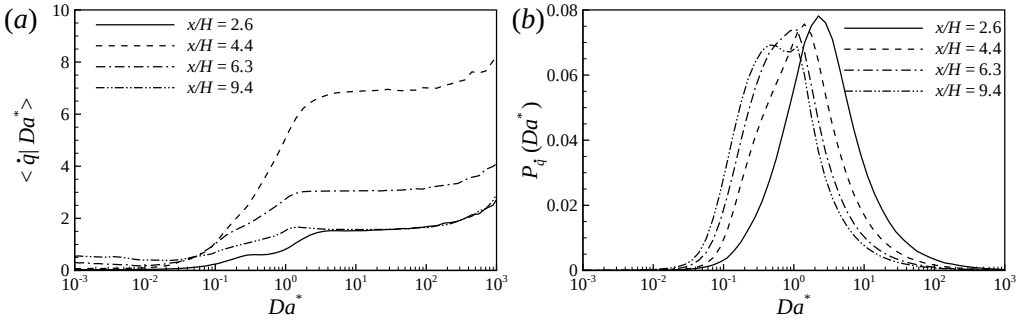

Figure 14: Axial variation of (a) mean heat release rate conditional on $Da = Da^*$ and (b) heat release rate-weighted PDF of Da with a cutoff value of $\dot{q} = 0.01$ J mm^{-3}s^{-1}.

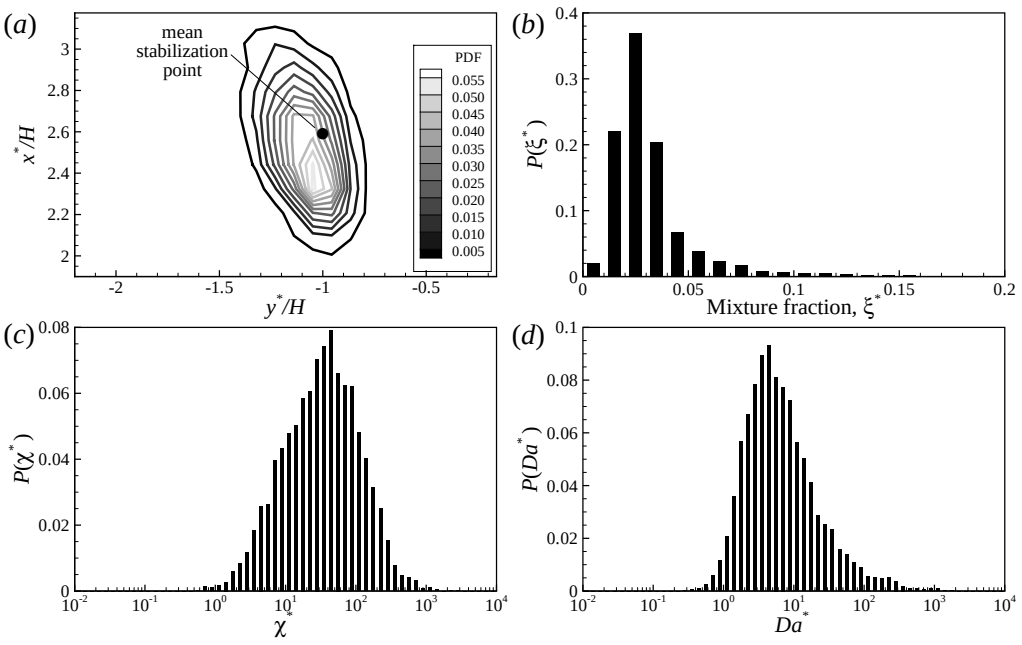

Figure 15: PDF of (a) the flame stabilization point, (b) mixture fraction, (c) scalar dissipation rate, and (d) Damköhler number at the local stabilization point.

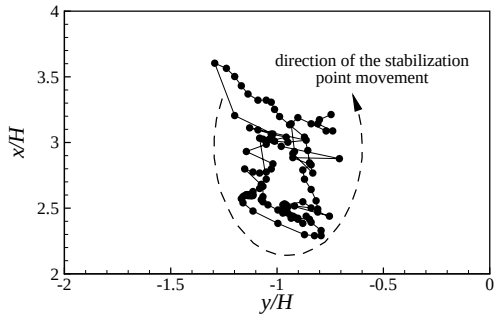

Figure 16: Scatter plot of the stabilization point location at $z = 0$ plane (left branch) from $t/\tau_j = 8$ to 12.

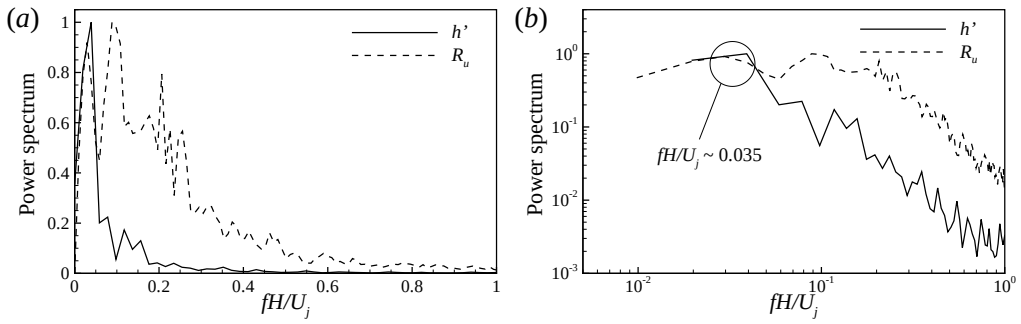

Figure 17: Power spectrum of the stabilization point fluctuation, h' and the correlation function, R_u: (a) in a linear scale and (b) log-log scale. The values are averaged over the homogeneous direction. f represents frequency.

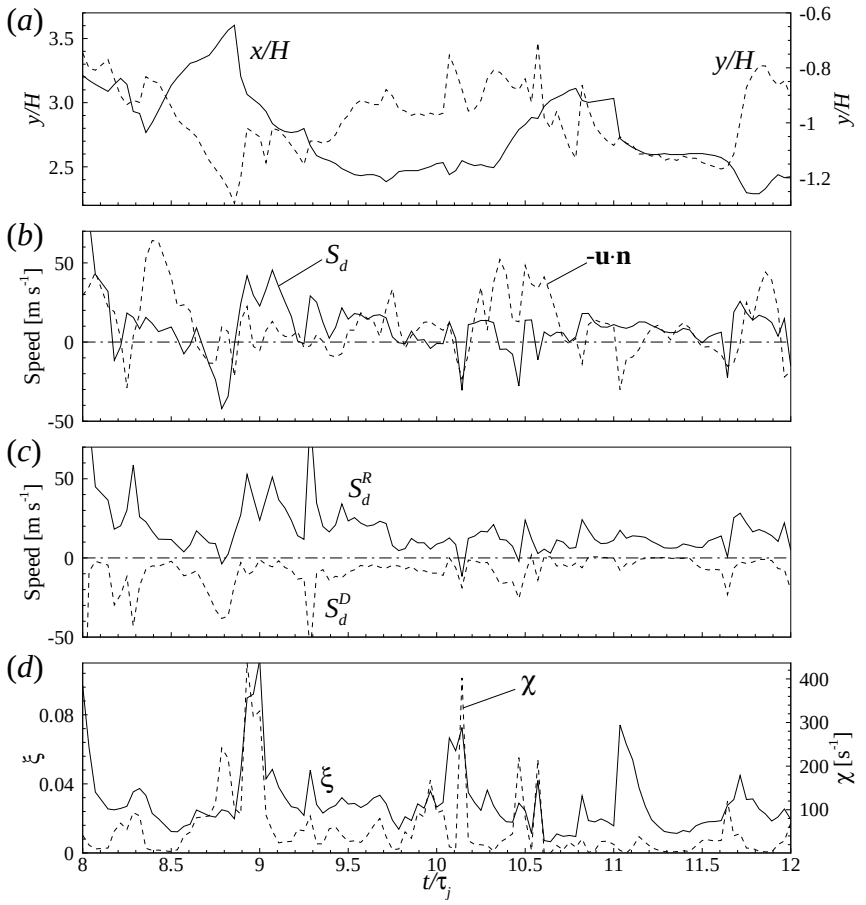

Figure 18: Temporal evolution of key scalar variables at the stabilization points at $z = 0$: (a) axial and transverse location, (b) flame-normal velocity and displacement speed, (c) S_d^R and S_d^D, and (d) mixture fraction and scalar dissipation rate.

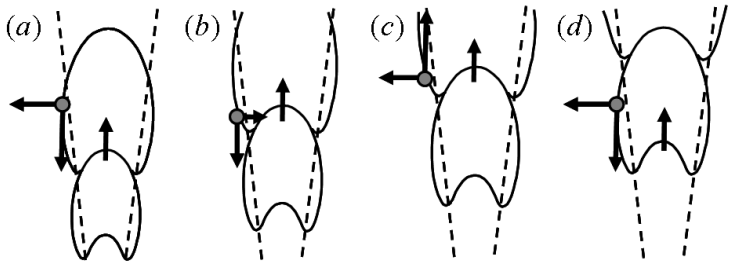

Figure 19: Schematic of the flame base movement in terms of the axisymmetric mode associated with large-scale organization of the mixing field (adopted from figure 20, Su *et al.* 2006): (a) ignition occurs in lean mixtures with low scalar dissipation rate, (b) the stabilization point propagates upstream following large flow structure, (c) the stabilization point is advected downstream by high axial velocity, and (d) ignition occurs in another large flow structure. Gray dot represents the stabilization point and dashed line denotes auto-ignition limit due to low temperature.